BUBBLE MEDIATED COPPER SUFACE MODIFICATION

BUBBLE MEDIATED SURFACE MODIFICATION IN THE COPPER ELECTROPOLISHING SYSTEM

By: ALLEN DANIEL PAURIC, B.Sc., B.Ed.

A Thesis Submitted to the School of Graduate Studies in Partial Fulfillment of the Requirements for the Degree Master of Science

McMaster University MASTER OF SCIENCE (2012) Hamilton, Ontario(Science)

TITLE: Bubble Induced Surface Modification in the Copper Electropolishing

System AUTHOR: Allen Daniel Pauric, B.Sc., B.Ed. (McMaster University)

SUPERVISOR: Professor Peter Kruse NUMBER OF PAGES: xi, 84

Abstract

Electropolishing is a commonly used method of mitigating surface roughness and yielding a polished appearance. One of the first described and most studied of electropolishing systems is the anodization of copper in phosphoric acid. Under normal conditions this reduces copper surface roughness substantially; however deviating from optimal electropolishing conditions can promote the development of semi-ordered surface roughness.

Anodizing copper substrates in 98-100% H_3PO_4 solutions generated feature heights ranging from 0.5 - 2µm and surface area increases in excess of 30% were obtained. The samples demonstrated a macroscopic optical dullness characteristic of this type of surface roughening. Investigations as to their applicability in surface enhanced Raman spectroscopy and electron field emission were conducted. And while their formation mechanism is still speculated on, it is believed that oxygen evolution and subsequent bubble formation plays a key role.

Electrochemical and microscopic imaging techniques were the primary methodologies used to probe the optical dulling phenomenon. With data obtained from experiments utilizing these techniques and others a qualitative mechanism is proposed.

Acknowledgements

In beginning this list of acknowledgements I would like to first thank Dr. Peter Kruse for allowing me to work under his supervision. The opportunity to conduct measurements on a wide variety of instrumentation has broadened my scope of physical chemistry. In addition his boundless optimism has been very helpful in getting through what at times has been a challenging project. I would also like to thank those I have worked with in the Kruse group especially Stephen, Tanzina, and Ali, their assistance is most appreciated and I hope I was able to return the favour.

An important acknowledgement goes out to Dr. Gillian Goward and Dr. Igancio Vargas-Baca whose critique and advice on my research has proven a valuable contribution. I would like to thank the many technicians and professors for trusting me with use of their instruments, and of course the wonderful office ladies especially Christine Cosgrove whom I have had to inconvenience on many occasions.

Finally I would like to thank my parents for the immense support they have given me over the years. A special mention goes to my girlfriend Nicole De Almeida whose 2 for 2 appearances in my theses acknowledgements section highlights her importance. Her support has been instrumental in getting me where I am today.

Table of Contents

List of Figures

List of Abbreviations

AC:	Alternating Current
AFM:	Atomic Force Microcopy
BZ:	Belusov-Zhabotinsky
DC:	Direct Current
NHE:	Normal Hydrogen Elecrode
NMR	Nuclear Magnetic Resonance
OER:	Oxygen Evolution Reaction
SCE:	Standard Calomel Electrode
SEM:	Scanning Electron Microscopy
SERS:	Surface Enhanced Raman Spectroscopy
XPS:	X-ray Photoelectron Spectroscopy

Chapter 1: Introduction

1.1 – Microscopic Topography and Material Properties

Solid surfaces that appear smooth to the human eye may possess degrees of surface roughness which vary by orders of magnitude. This micro and nanoscale topography inherent to all surfaces can impart a staggering array of different properties. Some examples include adhesion, corrosion resistance, reflectivity, reduced friction and many others.

A representative example of surface topography utilization is the adhesive properties of gecko feet. There are approximately 500,000 keratinous hairs known as setae on each foot. Each individual seta is 30 to 130 µm long with a width between 4 and 12µm. An individual seta terminates in several hundred spatula shaped projections at approximately 0.2-0.5µm in length.[1] The significance of this type of microscale topography is that it substantially enhances the surface area in contact with a substrate. This increases the number of short range Van der walls interactions and thus the total strength of the corresponding attractive interactions. An adhesive strength on the order of 10 N/cm^2 is typical.[2] It is this adaptation which allows geckos to climb vertical substrates including wood, rock, and even slippery substrates such as glass or Teflon. Synthetic analogues are currently being developed for human use.[3]

At the other end of the spectrum, the Gravity Probe B project had radically different topographic requirements. Its task was to detect and measure a phenomenon known as frame dragging. This phenomenon was theorized to be caused by the rotation of the earth. An analogy for this effect is that of a bowling ball spinning in molasses. The rotation of the bowling ball induces rotation of the molasses near it and thus any objects suspended in the molasses. As the earth spins it drags the spacetime around it including any satellites within it. In 1960, Schiff predicted that an ideal gyroscope would be able to detect such an effect as a precession in its rotation relative to a distant celestial reference.[4] In 2004, the Gravity Probe B satellite was launched containing four near perfect gyroscopes with the project concluding in the successful detection of the phenomenon.[5] The substantial accuracy necessary for the gyroscopes required an extraordinary degree of flatness to compensate for any precession caused by an imperfectly spherical gyroscope. Using ping pong ball sized gyroscopes of fused quartz with a thin layer of niobium the largest imperfections were kept at 10 nm and below. This made them the flattest man-made objects made at the time.

There are numerous other examples of surface topography having a direct impact on material properties. Given the usefulness of topographic control it is important to consider process methodologies that can yield the type of surface features desired. Of particular interest for the research in this thesis is the concept of altering surface topography through electrochemical means.

1.2 – Electrochemical Topography Modification

Traditional electrochemistry involves the application of a potential difference across two metallic electrodes immersed in an appropriate electrolyte. The difference in electric potential between the two electrodes changes the chemical potential at each electrode. This change in chemical potential can be used to promote redox reactions. It can also be of particular interest in efforts to modify the surface topography of the metallic electrodes.

Both deposition and dissolution are ways in which the surface of a metallic electrode can be altered. In deposition the electrolyte contains metal cations which are deposited at the electrode surface when an adequate reduction potential is applied. The cations can either be of the same composition as the electrode or different. In both cases the relevant deposition parameters can be altered to produce the desired structure. Research conducted by Bartlett et al. represents an example using template assisted electrochemical deposition to produce such desired structures.[6] They performed electrochemical deposition of gold and platinum films on polystyrene latex spheres (500-750 nm in diameter) assembled on a smooth gold electrode surface. Electric potentials of -0.90 and 0.10 versus SCE were applied for gold and platinum deposition respectively. This promoted metal cation deposition in the interstitial spaces between the polystyrene latex spheres. Subsequent dissolution of spheres through soaking in toluene left behind a highly ordered nanoporous film. Because the resultant pore diameters correspond to visible light wavelengths they diffract light readily and have potential applications as two-dimensional refractive elements.

Alternatively, a metal electrode can be run anodically to promote oxidation and subsequent dissolution. By varying relevant parameters e.g. electrode composition, electrolyte, and applied potential it is possible to obtain a wide range of different surface topographies. For instance, an alloy electrode composed of two different metals when subject to an anodic potential in the appropriate electrode will result in dissolution of one of the metals. The remaining interconnected porous framework of the undissolved metal is useful for applications where increased surface area is desirable e.g. catalysis and gas storage.[7]

A number of applications require smooth as opposed to roughened or porous substrates. This can be achieved down to sub-micron length scales via the process of electropolishing

1.3 – Electropolishing

1.3.1 – Overall Description

Anodic dissolution under certain conditions can result in an overall smoothing of surface topography in a process known as electropolishing. The electropolishing process was first patented and extensively described by Jacquet in the 1930s.[8] He was the first to demonstrate that anodic copper substrates in concentrated orthophopshoric acid could be microscopically smoothed without the aid of mechanical polishing. Extensions of this work include electropolishing of various metals and alloys e.g. stainless steel[9], niobium[10], titanium[11], and iron.[12] Stainless steel represents a common application of the process. It minimizes structural damage and impurity incorporation, polishing all surfaces in contact with the electrolyte.[13] This includes surfaces that may be inaccessible to mechanical polishing. Another application is found with regard to copper interconnects on integrated circuits. To function as an interconnect a copper surface must be planar. While chemical-mechanical polishing could be used it introduces scratches and mechanical stresses onto the substrate. Successful use of electropolishing would mitigate this type of substrate damage.[14]

1.3.2 – Basic Properties of Copper and Phosphoric Acid

Copper is a convenient model system for understanding electropolishing given the substantial body of literature collected to date. The nature of both the copper metal and phosphoric acid electrolyte are key to understanding how electropolishing arises under an applied anodic potential.

1.3.2.1 – Copper

Copper is considered a coinage metal which along with silver and gold in the same group possesses a similarly high corrosion resistance. The filled d shells of these elements contribute to their relative chemical inertness. Under conditions where copper does corrode, the development of a protective passive layer upon oxidation assists in inhibiting further corrosion. These factors contribute to copper being one of the few substances possible to be found naturally in its elemental state.[15]

Copper can be readily attacked by oxidizing strong acids such as nitric or sulphuric acid. The relative resistance of copper to oxidation is reflected in its standard reduction potential (0.34V for Cu^{2+} to Cu^{0}).[16] While copper can also oxidize to Cu^{1+} above 0.52V it is relatively unstable in aqueous solutions and disproportionates to Cu^{0} and Cu^{2+}. With respect to electropolishing, it is the reaction with phosphoric acid that is of interest.

1.3.2.2 – Phosphoric Acid

While considered one of the traditional strong acids, phosphoric acid is the weakest one the first proton dissociation pKa of 2.14. Given its relatively non-oxidising nature at room temperature it is often used in place of nitric or sulphuric acid where high acidity but low reactivity is desired. Typically, stock concentrated phosphoric acid is considered to be approximately 85% H_3PO_4 which represents an approximate 1:1 molar ratio of H_3PO_4:H_2O.[17] It possesses a number of unusual properties at high concentrations including an abnormally high electrical conductivity. Orthophosphoric acid is a relatively viscous fluid which under the basis of typical Stokes-Einstein diffusion should be substantially more resistive. However due to a highly interconnected hydrogen bonding network of orthophosphoric acid, protons can move between phosphoric acid molecules via a hopping mechanism.[18,19]

As H_3PO_4 content is increased the anomalously high conductivity is maintained in spite of further viscosity increases. Above 94% H_3PO_4 condensation of phosphoric acid monomers begins to yield diphosphoric acid. Longer chain phosphoric acid oligomers and even cyclic geometries appearing beyond 100% H_3PO_4. Research conducted in the 1950s investigated the relative proportion of phosphoric acid oligomers as a function of H_3PO_4 content.[20–22]

1.3.2.3 – Chemistry of Copper/Phosphoric Acid System

Copper readily dissolves in phosphoric acid. One can expect to find various ionic species during copper dissolution including Cu^{2+}, H_3O^+, and $H_2PO_4^-$.[23] However, the exact nature of the copper complexation is dependent on the concentration of the phosphoric acid. In dilute phosphoric acid water is the predominant complexing species. For typical stock concentrated phosphoric acid, the exact nature of the complexation is less clear though it is believed that water remains the primary acceptor species.[24]

A theoretical study using thermodynamic equilibrium for copper in phosphoric acid was conducted by Aksu[25] to determine the speciation of copper under various conditions of applied potential and pH. When plotted in the form of Pourbaix diagrams the equilibrium confirmed that under conditions of low pH and high applied potential, Cu^{2+} is the predominant species. Additionally, the low pH associated with high H_3PO_4 concentration allowed for phosphoric acid to act as proton acceptor yielding $H_4PO_4^+$ with a pKa of zero. The chemistry becomes increasingly more complex with further increases to phosphoric acid concentration. The lack of water and the appearance of polyphosphate species adds an extra dimension to copper speciation. Unfortunately, there has been relatively little research performed on copper chemistry under such conditions.

1.3.3 – Electropolishing Mechanism

The specific mechanism of electropolishing was described in a review by Landolt.[26] For smoothing to occur there is the requirement for the formation of a resistive surface layer which can moderate dissolution rate. Taking the copper/phosphoric acid electropolishing system as an example the formation of the resistive regime can be identified by the mass transfer limited current plateau observed in Figure 1. This behaviour can be explained by considering the local environment surrounding copper dissolution. Specifically, as the dissolution rate increases there is a local reduction in water concentration as well as an accumulation of dissolution product. The layer thus formed is considered a passive layer as it is no longer electrochemically active but it significantly increases the local viscosity and electrical resistivity. This promotes mass transfer control of the dissolution reaction which is the basis of electropolishing.

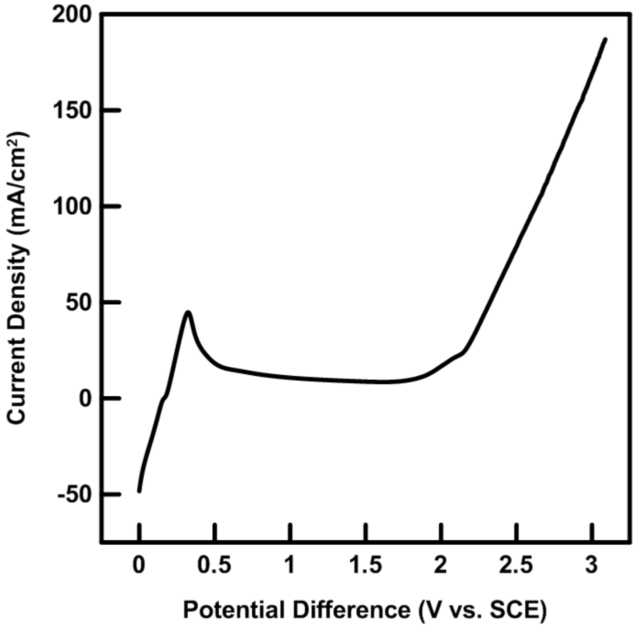

Figure 1: Linear voltammagram of copper anodization of 86% H_3PO_4 at 20°C

Anodic brightening occurs at length scales below 1 micron, comparable to the optical wavelengths. Characteristic to it is the mitigation of crystallographic etching. Specifically, under normal circumstances certain crystal faces are more favourably dissolved over others. The anisotropic etching that this entails leads to a rougher surface at the sub-micron scale. With the presence of a passive layer, dissolution changes from a kinetic to a mass transport controlled process. The favourability of certain crystal faces to dissolve is outweighed by the limitation on solubility caused by the resistive surface layer. Dissolution thus occurs when an opening in the passive film is present, promoting isotropic etching and a smoother topography. Another mechanism of microsmoothing is that of preferential dissolution of surface asperities. The locally thinner film at surface asperities promotes a locally higher current density resulting in the micron scale polishing observed.

There still exists substantial debate surrounding various aspects of the mechanism of copper electropolishing. One contentious issue is the identity of the acceptor species. The current prevailing theory is that diffusion of water towards the anode is the rate limiting step.[23,24,27] It enables transport of copper ions within the surface film to diffuse into the bulk, allowing continued anodic dissolution. An alternative theory suggests that copper continues to dissolve until the solubility of a copper salt is reached, at which point it precipitates back onto the anode and mitigates further dissolution as a solid film.[28–30]

1.4 – Oxygen Evolution

Literature discussing electropolishing chemistry after the onset of anodic oxygen evolution is relatively sparse. Oxygen evolution tends to facilitate pitting corrosion and reduce the polish quality. It is a competing reaction which masks the anodic current originating from metal dissolution. As a result electrochemical characterization is made more difficult. Also, the generation of oxygen bubbles complicates the use of various imaging and spectroscopic techniques. Given that the region beyond the start of oxygen evolution is difficult to study and of little industrial importance, the lack of research in the area is unsurprising.

In spite of this the primary focus of this thesis lies precisely in the oxygen evolution regime. Surface topography deemed undesirable towards electropolishing applications is itself a phenomenon that can be further understood and manipulated. Therefore, the following is meant as an introduction to oxygen evolution and subsequent bubble formation. These can later be linked to electrochemical and topographical changes at the anode.

1.4.1 – Oxygen Evolution Reaction (OER)

Oxidation of water to oxygen is a four electron process which occurs by the following overall mechanism in acidic media.

$$2\ H_2O_{(l)} \rightarrow O_{2(g)} + 4H_{(aq)}^{+} + 4\ e^{-}$$

With a standard reduction potential of 1.23 V vs. NHE the OER requires a substantial applied potential difference to proceed. The liberated protons are typically reduced to hydrogen gas at the cathode.

$$4H_{(aq)}^{+} + 4e^{-} \rightarrow 2\ H_{2(g)}$$

In phosphoric acid media this process is assisted by the efficient conduction of protons to the cathode, resulting in relatively vigorous oxygen evolution.

The relative simplicity of the overall equation for the OER betrays the substantial complexity surrounding the reaction. A general reaction scheme hypothesis as outlined in a review on the subject by Dau et al.[31] involves the dissociative adsorption of water to form surface hydroxide. This is followed by loss of the remaining hydrogen and finally recombination of surface oxygen species to evolve oxygen gas. Unfortunately there is little evidence to test potential hypotheses against due to a lack of direct spectroscopic observation of reactive intermediates. Research thus far has generally relied on indirect electrochemical characterization which while insightful has been unable to provide conclusive evidence on the specifics of the reaction.

1.4.2 – Bubble Formation

When the volume of oxygen evolved during water oxidation surpasses the solubility limit of the surrounding electrolyte, the excess oxygen nucleates at favourable sites on the anode surface. There are a number of factors which contribute to the favourability of a particular site including the local topography. Generally, bubble nucleation will tend occur in cracks, fissures, pores or other surface depressions. [32] As bubbles grow from their nucleation sites they adhere to the electrode surface and eventually depart upon reaching their departure radius. From this develops the equilibrium fractional bubble coverage Θ . This describes the fraction of the electrode surface shadowed by surface bubbles.[33]

Adhering bubbles have the effect of shielding the area immediately underneath them from the surrounding electrolyte, preventing that section of electrode from participating in redox reactions. This effect is often balanced however by the convection generated upon the departure of a bubble from the surface. The reduction in active surface area causes the measured superficial current density to be lower than the actual current density. This relationship between superficial and actual current density is accounted for with the following equation.[33]

$$j = \frac{I / A}{1 - \Theta}$$

Bubble coverage fraction is but one method of describing bubble properties. There exist numerous other aspects to consider when trying to quantitatively describe bubble dynamics including size, velocity, contact angle, and electrolyte viscosity. Given the myriad of variables, analytical challenges, and inherent randomness, a comprehensive quantitative model becomes difficult to achieve. Nevertheless the influence that bubbles have on current density from both a magnitude and spatial perspective merit consideration

1.5 – Pattern Formation During Electropolishing

While electropolishing functions well in eliminating large scale surface roughness, topography at length scales less than 100nm are not necessarily smooth. Regular surface features including stripes, dots, dimples, waves can be observed.[34,35] They are believed to originate from the presence of a closely packed double layer of solvent molecules and ions, also referred to as a Helmholtz layer of approximately 10 nm in thickness. This layer is in addition to the already present surface layer which can be up to a micron in thickness. Because of the difference in length scale the same processes that cause surface smoothing above 100 nm do not have the same effect at smaller length scales. Instead, the Helmholtz layer dominates the dissolution pattern. A proposed theory is that there is preferential adsorption of polar or polarizable chemical species at the rough sections of the substrate due to an enhanced electric potential.[36] The adsorbed species shield the raised sections from dissolution, promoting the development of a raised surface topography. However, very small variations in the applied electric potential can have a dramatic impact on adsorption affinity thus changing the observed surface patterns.

Characteristics of spatiotemporal patterns formed in chemical systems are the domain of nonlinear chemical dynamics. Nonlinear systems are defined by behaviour that does not depend linearly on one or more key variables. The prototypical example of nonlinear behaviour is the oscillatory reaction. Believed to be in violation of the second law of thermodynamics for much of the twentieth century, the Belousov-Zhabotinsky (BZ) reaction is a well known oscillatory reaction.[37] It is multistep reaction which periodically oxidizes and reduces the redox indicator ferroin. This yields a solution which alternates in colour between the oxidized blue ferrin and the reduced red ferroin. In unstirred conditions this can even yield alternating red-blue spirals in an initially homogenous solution. Oscillatory reactions are not restricted to bulk solution phase chemistry. They can be observed on solid surfaces as well. Our own group has investigated step formation on nickel as caused by the cyclical build-up and dissolution of nickel sulfate on anodized nickel wire in concentrated sulfuric acid.[38] Each current spike observed in the chronoamperometry data was temporally correlated to the formation of an individual step on the nickel substrate.

As discussed by Turing[39] spatiotemporal patterns in chemistry can be described by a reaction-diffusion mechanism. Whether oscillatory in nature or otherwise they are influenced by the relative rates of reaction and diffusion and how they vary spatially and temporally. Understanding how these two parameters are influenced is important to describing pattern formation in nonlinear chemical systems.

A significant focus of our group has been to observe and describe the formation of ordered patterns on metal surfaces during electropolishing. One pattern in particular are the ordered arrays of nanoscale dimples observed on various metal substrates.[40,41] However the electropolishing conditions used involved hydrofluoric acid (HF). The use of HF limits the types of in-situ characterization that can be safely employed. Attempts were made to switch to a system which did not contain HF but could still yield dimples. Copper being a well-studied electropolishing system represented a potential candidate for HF free dimple formation. Unfortunately dimples were not observed; instead large micron scale semi-ordered patterns developed which had similarities with but were ultimately distinct from dimple formation.[42,43]

1.6 – Thesis Objectives

The focus of this thesis is concerned with investigation of a phenomenon which has hitherto been undescribed. Specifically it involves the breakdown of electropolishing conditions for the copper/phosphoric acid electropolishing system. This yields a micron scale patterned surface roughness within a specific H_3PO_4 concentration range. The study aims to first describe the general characteristics of the obtained surface along with a discussion of potential applications. Following this a mechanistic study of the phenomenon will be presented with the goal of proposing potential explanations. Ideally this thesis will serve as an introductory study which lays the groundwork for any further investigations into the phenomenon.

Chapter 2: Methodologies and Procedures

2.1 – Methodologies

2.1.1 – Electrochemical Characterization

2.1.1.1 – Choronoamperometry

Application of a potential difference can be used to drive an electrochemical reaction. Measurement of the current obtained while maintaining a constant potential over time is known as chronoamperometry. The technique is especially useful for characterizing electrochemical processes which evolve over time. The current density obtained can allow for the determination of corrosion rate, however it is limited to showing the total value for current density. As such, simultaneously occurring reactions such as metal dissolution and gas evolution cannot have their relative current contributions differentiated by chronoamperometric data alone. Circumventing this limitation involves measuring the volume of gas evolved to calculate the current fractions.

The gas volume measured can converted to a mole based quantity through the ideal gas law.

$$n = \frac{PV}{RT}$$

Oxygen gas is only evolved through water dissociation which is a four electron process. Utilizing Faraday's constant and factoring in the time elapsed to produce the measured gas volume the oxygen evolution current can be obtained.

$$i_{O_2} = \frac{4 \cdot n_{O_2}}{t} \cdot 96485\ C/mol$$

Subtracting the oxygen evolution current contribution from the total yields the copper dissolution current.

2.1.1.2 – Electrochemical Impedance Spectroscopy (EIS)

Resistance is the property of a circuit element which resists the flow of electrical current. However Ohm’s law only concerns ideal resistors and as such has certain simplifying assumptions. When dealing with AC circuits the simplifying assumptions can no longer be used and one must consider impedance instead. A simple EIS experiment involves the application of a small, sinusoidal AC excitation to a sample, often superimposed on a DC bias potential. The oscillating AC potential generates a corresponding sinusoidal current response. However, depending on the electrical impedance inherent to the sample, there will be a lag in the current response. This delayed response is represented by the phase shift of the current relative to the AC potential applied. Using Eulers relationship and an analogous expression of Ohm’s law the total impedance can be described.

$$Z(\omega) = Z_0(\cos\phi + j\sin\phi)$$

The $Z(\omega)$ term is the total impedance as a function of the radial frequency of the AC sine wave. This function has a magnitude component Z_0 which is the ratio of applied voltage to current and a phase shift component $\cos\phi$ and $j\sin\phi$. Plotting $Z_0 j\sin\phi$ versus $Z_0\cos\phi$, more commonly referred to as Z'' and Z' yields the Nyquist plot used for representing impedance data. The Z' value represents the real resistance of the circuit whereas the imaginary Z'' value is the reactance of the circuit, which can be used to determine capacitance.

When describing an electrical system using impedance spectroscopy, it is often modeled as an equivalent circuit, with a series of resistors and capacitors in parallel. Factors such as electrolyte and polarization resistance contribute to the resistive elements of the circuit whereas the electrical double layer contributes to the capacitive elements. The classic semicircle typically observed in an EIS spectrum is a consequence of the combination of the resistive and capacitive elements. At very high AC frequencies, capacitors act like a short circuit. The AC current can traverse the capacitor with minimal impedance. Thus, the high frequency end of an impedance plot is observed at the low resistance portion of the Z' axis. The resistance it begins at is determined by the resistance of the connections to the electrochemical cell and importantly the resistance of the electrolyte. As the AC frequency is decreased more resistance is encountered in the capacitive elements. The Z'' value increases to a maximum where it can be used to determine the actual capacitance along with the Z' value as the capacitor becomes more resistive. At very low frequencies the capacitor becomes more resistive than the original resistive elements, thus the electrical current passes through the resistive elements instead.

Many impedance spectra are not as simplistic as one semicircular arc however. They often involve multiple relaxation processes occurring simultaneously. Fortunately, there is at least partial separation of their impedance responses due to the difference in relaxation time and the frequency dependent nature of EIS. Nevertheless multiple impedance features will often overlap, making the interpretation of the impedance spectrum substantially more difficult. Such considerations highlight both a strength and drawback of EIS. Specifically, complex systems with multiple simultaneous reactions can be characterized and modeled. Unfortunately this model can be ambiguous and subject to misinterpretation.

2.1.2 – Imaging Techniques

2.1.2.1 – Atomic Force and Scanning Electron Microscopy

AFM is a simple but versatile imaging technique which relies on a direct contact interaction between a nanoscale tip and the substrate. The force applied to the tip and tip height above the substrate are measured to enable rastering across the surface and yield a topographical map.[44] There are various operating modes for AFM including contact, tapping and non-contact mode. While they have certain advantages and disadvantages associated with them, the mode selected will depend on the sample being probed. AFM can be performed under a wide range of ambient conditions including in liquids. However, care must be taken when interpreting images collected with AFM. The quality and resolution of the images are directly related to tip size and quality. Damage to the tip can cause significant image distortion. Additionally, AFM is a slow technique relative to SEM, with good images requiring over an hour to acquire. Nevertheless, its versatility and flexibility make AFM a particularly useful imaging tool.

SEM complements AFM in that it is useful for the acquisition of large microscale images in a short time frame. However, it cannot yield quantitative depth information as an AFM can and generally tends to have somewhat less resolution than an optimized AFM system. It operates by firing electrons at a specific accelerating voltage onto a sample that is inherently conductive or made conductive via sample preparation.[45] Secondary electrons ejected as a consequence of the electron impact are typically used to construct an image of the surface. An advantage of this method is that the image does not have tip size and shape limitations like in AFM. Though electronic properties of the sample may impact the image contrast and otherwise distort the image.

2.1.3 – Spectroscopic Techniques

2.1.3.1 – Nuclear Magnetic Resonance (NMR)

An NMR measurement takes advantage of the non-degeneracy of nuclear spin states for a nucleus in an applied magnetic field.[46] When the magnetic nuclear spins of a sample are precessing about an applied magnetic field, a radio frequency pulse is used to excite the nuclei and rotate the nuclear spins away from equilibrium. The radio waves emitted from the nuclei as they relax to their initial state are used to construct an NMR spectrum. Nuclei in different chemical environments can be distinguished because of the shielding from electrons surrounding them. This causes an NMR spectrum to often be composed of multiple peaks reflecting the distribution of electron density around the nuclei. Information gained from this phenomenon is particularly important to chemical identification and quantification and can even allow for the study of molecular dynamics.

2.1.3.2 – X-ray Photoelectron Spectroscopy (XPS)

Instrumental techniques involving photoelectrons use incident photons of sufficient energy to eject electrons from the elements comprising the substrate. When this is performed with x-rays the energy is sufficient to eject core electrons from the electronic shell. The core electrons have an element dependent binding energy which can be calculated based on the kinetic energy of the ejected electron. While electron binding energy is mostly influenced by the columbic interaction between the electron and nucleus, the exact value can be weakly influenced by the local electronic environment. Specifically, for elements which possess excess electron density the electronic shielding effects lowers the strength of the internuclear attraction, thus lowering the electron binding energy. The degree of electronic shielding is dependent on the interatomic environment and the relative electronegativities of the constituent elements. Slight changes to the binding energy can thus yield qualitative information on the chemical environment. Additionally, XPS can be used in a semiquantiative manner by comparing the relative peak area of different signals against each other. Quantitative measurements are made difficult because of various factors ranging such as sampling angle and variable background fits which lower the total number of photons detected. While this isn’t a problem if proportional data is desired, quantitative measurements require a substantial amount of effort to achieve any reasonable degree of accuracy.

XPS is a surface sensitive technique due to the short mean free path of the ejected electrons. This means that generally only the first 10 nm of the surface is sampled.[47] In addition, the short mean free path generally necessitates the use of ultra high vacuum conditions to allow for the detection of the photoelectrons. One drawback to XPS is the necessity for substantial peak deconvolution. Specifically, the binding energy differences between different states of the same element often result in significant peak overlap, making peak fitting procedures challenging.

2.1.3.3 – Spectroscopic Ellipsometry

When trying to measure the physical properties of complex, multilayer samples, spectroscopic ellipsometry is often used. The basic principle underlying it concerns measuring changes in the properties of polarized light upon reflection from a sample. Specifically these parameters (ψ,Δ) correspond to the amplitude ratio and phase difference between s and p polarized light waves respectively. In addition, the wavelength of light can be varied from ultraviolet through visible and into the infrared region to obtain information on a wide range of physical characteristics. These can include film thickness, band gap values, conductivity, and phase structure among many more.[48] While it is heavily reliant on proper fitting procedures to produce such data, adequate care taken during measurement and fitting can aid greatly in improving its reliability.

2.1.3.4 – Raman Spectroscopy

The fundamental principle underlying Raman spectroscopy is the Raman effect which involves the inelastic scattering of light. One out of every 10^6-10^8 photons encountering a molecule will inelastically scatter. This highlights the relative inefficiency of the Raman effect. When a molecule does inelastically scatter however, this usually means the light is red-shifted by the energy necessary to cause the excitation of a vibrational mode. The difference between the initial laser light and the lower energy Raman scattered light is also known as a Stokes shift. Alternatively a photon can encounter an already excited molecule and be blue-shifted as it gains energy from a relaxing excitation, characteristic of an anti-Stokes shift. This phenomenon can yield a spectrum of the different vibrational modes characteristic to the sample.[49]

As an analysis technique, Raman spectroscopy is relatively non-destructive and works in a variety of sampling geometries. The monochromatic laser used as an excitation source can be tuned to different wavelengths as suits the sample. Also, because it functions via light scattering it can be used with opaque solids and even through electrochemical cells to monitor a reaction in-situ. However, it is somewhat limited in its sensitivity due to the inefficiency of Raman scattering. To compensate for this, one can employ substrates conducive to surface enhanced Raman spectroscopy (SERS).

The SERS effect has the capability to enhance the Raman signal from a molecule by many orders of magnitude. Additionally, this molecule will show additional vibrational modes arising from its interaction with the substrate. For studies of surface reactions, the enhanced sensitivity and surface selectivity are invaluable. However, large SERS enhancements in the optical range are only observed on coinage metals (copper, silver, gold) which possess nanoscale features on the order of 5-100 nm in size. Reasons for limitations on the SERS effect originate from details regarding its mechanism.[50]

Two enhancement mechanisms operate under SERS, the electric and charge transfer effects with the primary enhancement mechanism being the electric effect. The electric effect originates from surface plasmons which are quanta of plasma oscillations, electrons in this case. Surface plasmons are excited by the electric field component of an incident light wave. The valence electrons weakly attracted to the nucleus are responsible for the oscillating surface plasmon. If the incident light is in resonance with a dipolar surface plasmon the metal substrate can emit light of the exciting wavelength at an enhanced intensity onto the surface molecules. In addition to enhanced light intensity at the molecule, some of the Raman scattered light can be scattered toward the metal particle and then reemitted at a higher intensity. Charge transfer enhancement is somewhat more controversial but likely has to do with the binding to a metal surface allowing for more optical transitions via interaction with the conduction electrons. The greater number of polarization routes increase the probability of a Raman excitation.[51]

2.2 – Procedures

2.3.1 – Substrate/Experimental Conditions

Sample preparation was based on deviations from electropolishing conditions. High purity copper substrate (>99.99% Cu – Sigma Aldrich) was first ultrasonically cleaned sequentially for 10 minutes in acetone, water, and methanol. Either cylindrical copper wire or flat copper sheets were used depending on the specifics of the experiment. The substrate was then anodized in concentrated phosphoric acid with a concentration ranging from that of orthophosphoric acid (~86% H_3PO_4 – Fischer Scientific) to polyphosphoric acid (~116% H_3PO_4 – Sigma Aldrich). Intermediate phosphoric acid concentrations were developed by mixing appropriate amounts of orthophosphoric and polyphosphoric acid with stirring for several days. Significant stirring times were necessary to accommodate for the high viscosity and thus slow equilibration of the solution. For temperature controlled anodization a thermostated water bath in combination with a jacketed beaker was used for temperature control to within 1^{o}C ranging from 10^{o}C to 90^{o}C.

2.3.2 – Anodization Conditions

The copper substrate was subjected to anodization at potential differences ranging from 0-6V. However a representative voltage of 6V was often chosen as an independent variable to observe topographic changes upon changing other relevant variables. For those samples which did not require particularly accurate voltage control an Agilent E3617A DC power supply was used to supply an overall cell voltage to a two electrode configuration. However because the potential at the counter electrode is not constant the actual voltage of the copper anode was known to be up to 1V less than the value for the overall cell voltage. For those experiments which required more accurate voltage control a three electrode setup was used with a Ag/AgCl reference electrode at 200 mV versus NHE. The potential of the reference electrode is designed to remain constant. This is achieved through the use of an enclosed redox reaction separated from the surrounding electrolyte by a porous plug. It can thus be used to determine the exact working electrode potential. Voltage control of the three electrode setup was performed with an Autolab PGSTAT30 potentiostat.

Anodization was generally performed at the desired voltage for 8 minutes. Separation of copper dissolution and oxygen evolution involved the use of a plastic syringe to collect and measure the evolved oxygen gas. As shown in figure 2 the syringe was filled and inverted with a copper wire anode of known length and diameter placed underneath. Other parts of the wire were insulated in plastic to prevent dissolution at areas not underneath the syringe. The volume of the displaced electrolyte from the syringe represented the volume of gas evolved from the anode.

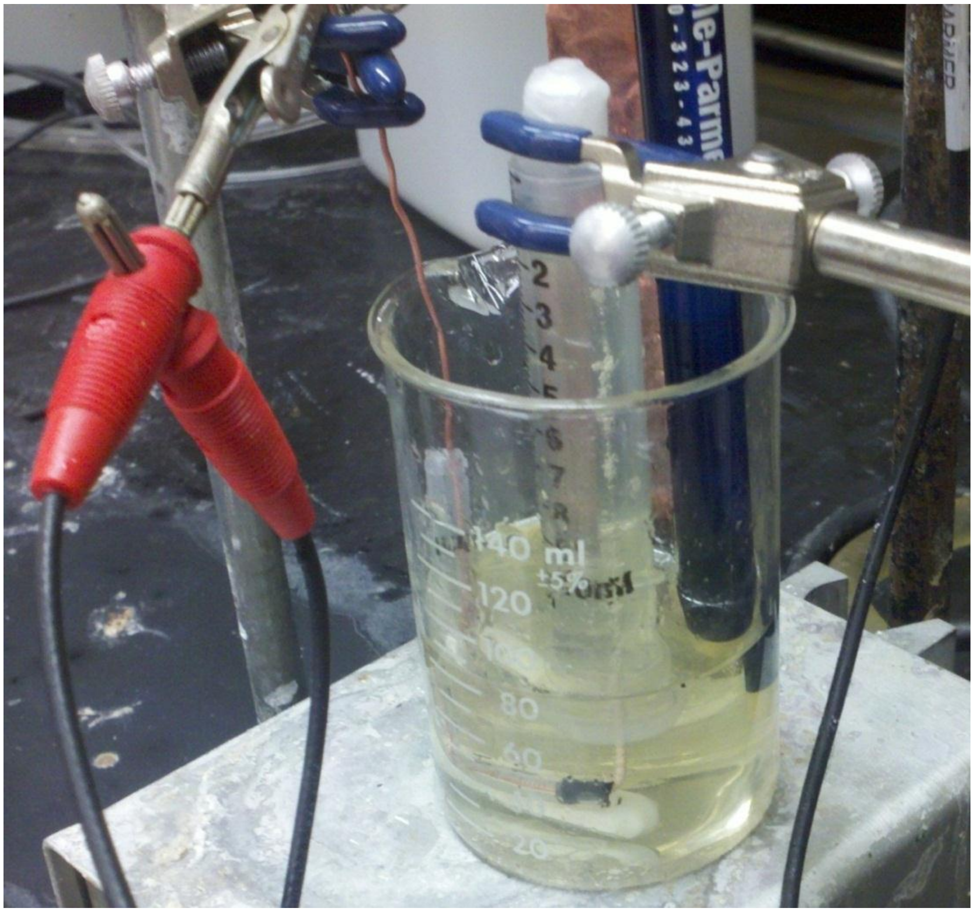

Figure 2: Experimental Setup for the Separation of Oxygen Evolution and Copper Dissolution Current Contributions

Orientation was varied for some experiments to observe its effect on surface topography. Post-processing involved ultrasonic cleaning for 2 minutes sequentially in 1M H_2SO_4, water, and methanol. The samples were then allowed to dry and stored in air.

2.3.3 – Instrument Parameters

EIS measurements were obtained with a Solartron 1252A/1280 Frequency Response Analyzer/Potentiostat-Galvanostat. The applied potential ranged from 1-8V and was referenced to an Ag/AgCl reference electrode. Phosphoric acid concentration was varied from 86 to 105% H_3PO_4. Data was collected and processed with the Zplot/Zview software suite. Due to the noisy conditions encountered during vigorous oxygen evolution a large AC amplitude of 50 mV was used to enhance the signal to noise ratio. Additionally, a three minute pre-treatment at the experiment voltage was used to allow the system to attain a stable current value. Frequency measurements were performed across a logarithmic scale from 300,000 to 1 Hz with average experiment duration being approximately 15 minutes.

AFM images were collected on a Veeco Digital Instruments Enviroscope with a Nanoscope IIIA controller in contact mode with a non-conductive DNP-S10 silicon nitride pyramidal tip (Veeco Insturments). While contact mode yields poor horizontal spatial resolution in comparison to tapping mode AFM the large scale topography characteristic to the measured samples made the additional resolution unnecessary. However, the silicon nitride tips are more resilient and less prone to breakage than tapping mode tips. In addition, copper surfaces are not easily deformed by the forces applied during AFM and thus are well suited to contact mode imaging.

SEM was conducted as compliment to the AFM data and was performed on a JEOL JSM-7000F Field Emission SEM. Clean samples were placed onto a stainless steel sample stub and fixed in place using conductive carbon tape. In some cases, conductive silver paste was also used to further ground the samples and mitigate detrimental charging effects. Raman spectroscopy was performed with a Renishaw inVia Raman microscope including a 785 nm laser source, 50x objective lens, 1200 l/mm grating with the Renishaw Wire 3.2 acquisition software. This was typically performed at 10% of the maximum laser power on a spot size 1 micron in diameter.

High speed camera images were taken using a Troubleshoot model camera from Fastec Imaging (2007). This was done in the horizontal substrate geometry at a resolution of 640x480 pixels with 20x microscope objective lens. This corresponded to an image width 400 micron across.

Chapter 3: Results

3.1 – Phenomenon Description

Shown in figure 3 are three copper substrates anodized at 6V cell voltage for 8 minutes. They were anodized at three slightly different H_3PO_4 concentrations in a vertical geometry. These are all shown in comparison to a bare copper substrate. There is a clear change to the observed topography upon anodization at the appropriate phosphoric acid concentration. The etching effect observed is substantial enough to be observable macroscopically as an optical dulling of the sample (Figure 4). This is a consequence of the increase in scattering as caused by the increased surface roughness.

Variability in the copper surface obtained with slight changes to experimental parameters is clearly identified. The topography at 98% H_3PO_4 shows the extent to which an ordered surface pattern develops. A wavelike semi-ordered pattern is clearly visible at sub-micron length scales. Increasing the concentration to 99% yields surface features at approximately the same 0.5 µm height scale but the depressions have increased in size. At 100% H_3PO_4 however the wavelike pattern disappears but the depth of the surface features increase. Surface area estimates by AFM indicate a minimum surface area increase of 30% over bare copper. The actual area however is likely higher due depth limitations imposed by the tip from its physical dimensions

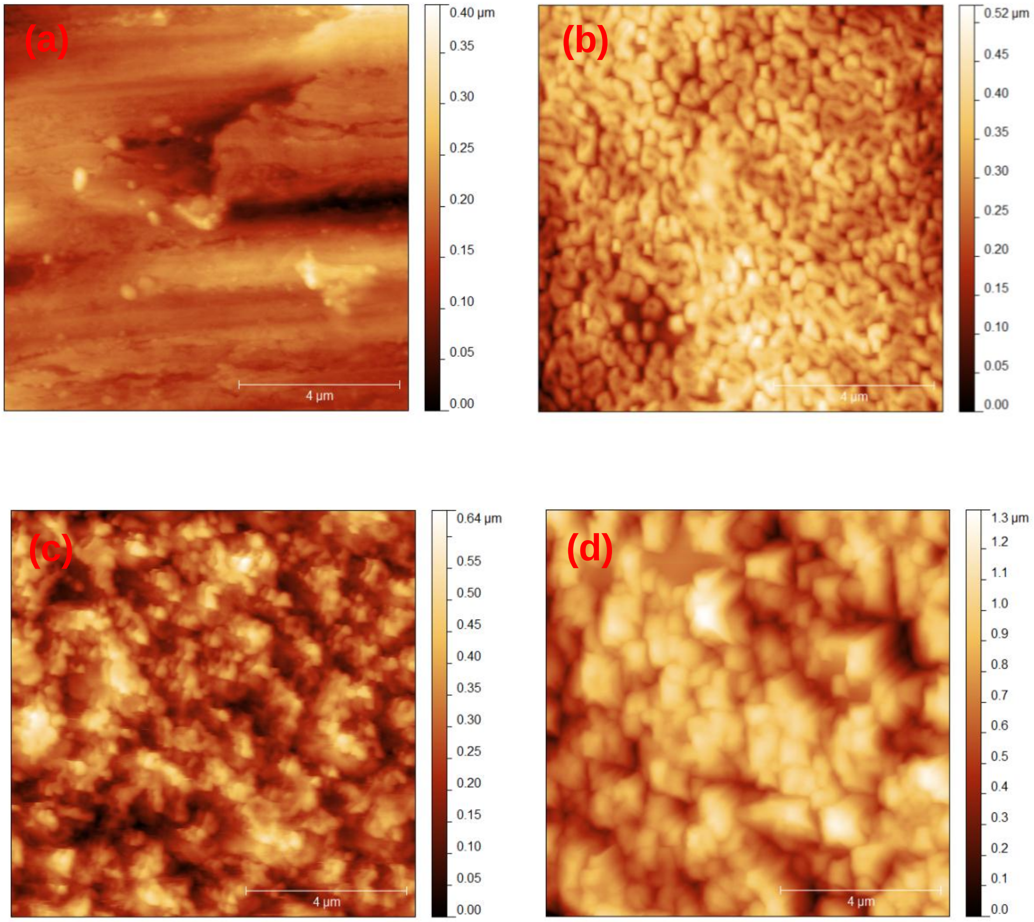

Figure 3: Bare copper wire (a), and copper wire anodized in 98 (b), 99 (c), and 100 (d) %H_3PO_4 acid at 40^{o}C anodized at 6V cell voltage for 8 min in a vertical geometry

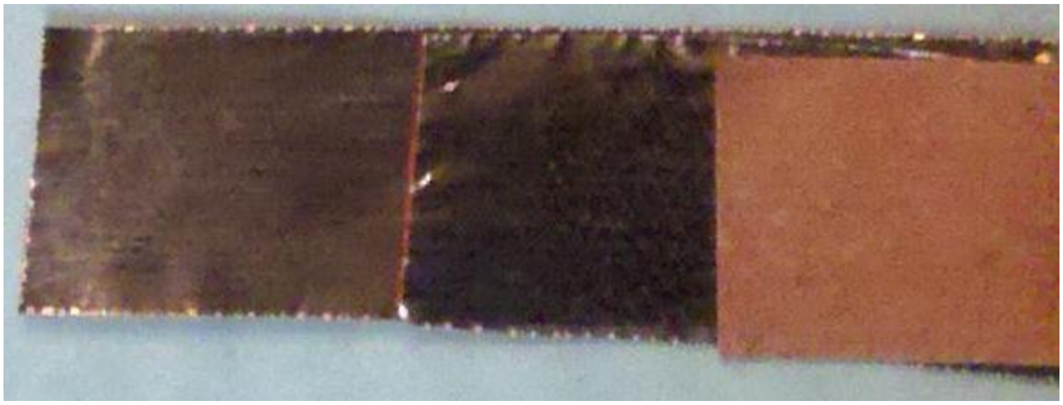

Figure 4: Optical comparison of unmodified copper substrate (left), electropolished substrate (middle), and optically dulled substrate (right)

A more comprehensive investigation on the concentration dependence of the observed copper surface patterning is detailed in figure 5. They demonstrated that substantial surface features are only observed within a narrow concentration range. Lower concentrations yield electropolishing while higher concentrations have insufficient water content to enable significant dissolution. From a combination of SEM and AFM images in combination with macroscopic observations it was determined that the most substantial etching occurs between approximately 98-100% H_3PO_4.

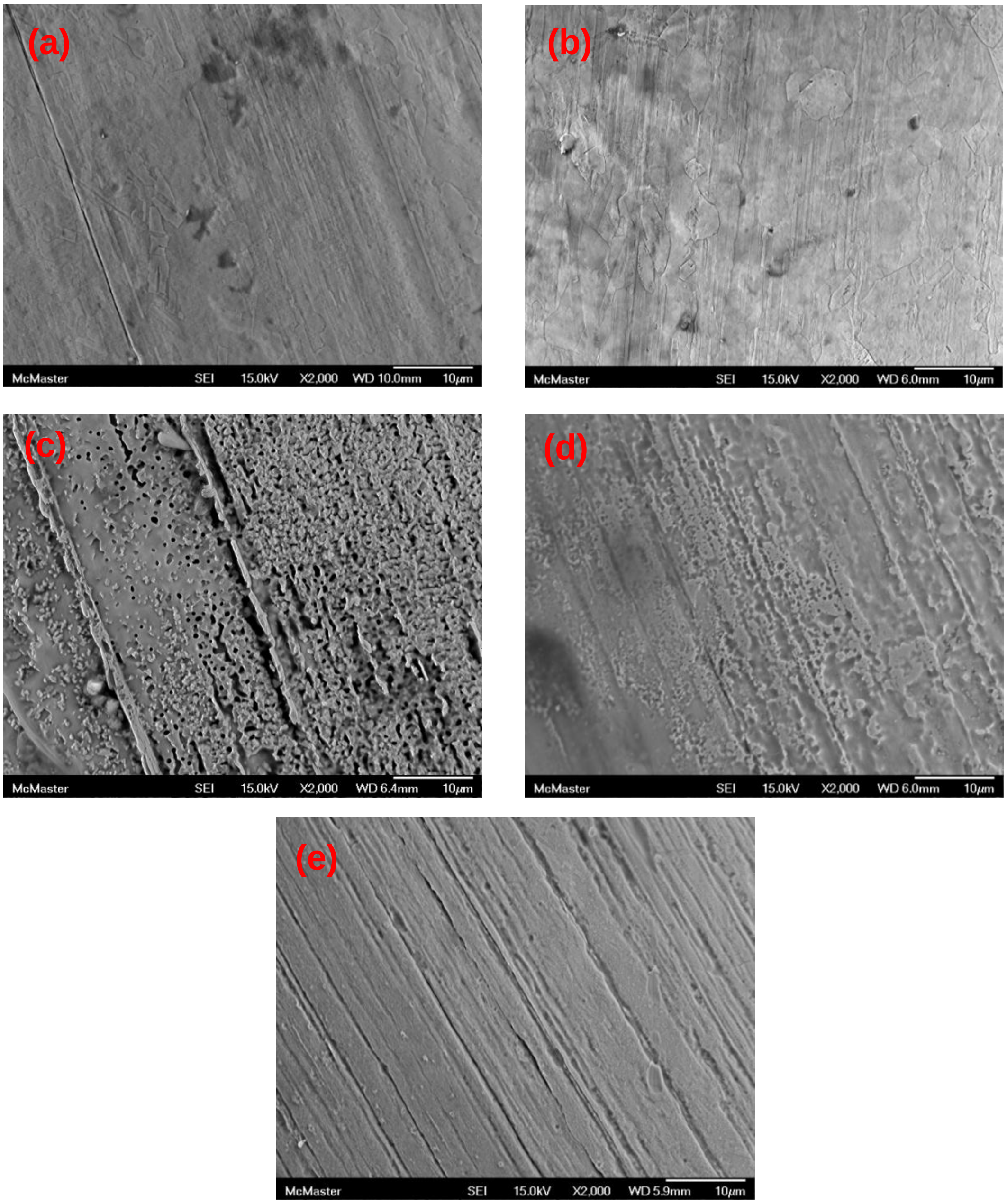

Figure 5: SEM pictures of vertical copper wire substrates anodized at 6V cell voltage for 8 min in 40^{o}C H_3PO_4 at concentrations of 86% (a), 95% (b), 100% (c), 102.5% (d), and 116% (e)

The surface roughening and consequent optical dulling observed has thus far not been described in the available literature. Though this is unsurprising because of the conditions under which it is observed. Specifically, these include the requirement for a high H_3PO_4 concentration and a potential above 3V versus SCE. As these conditions are in a regime which has few applications it has remained relatively unexplored. However, the relative lack of research in the area represented an opportunity for novel research.

Temperature was added as an additional variable to observe its effect at a known concentration (Figure 6). Initial dissolution at room temperature tends to be directional along the machining lines already present on the copper wire substrate. Increasing electrolyte temperature produces a more disordered surface topography which transitions back to an electropolishing regime at even higher temperature. Of particular note was that at sufficiently high temperature a spiral dissolution pattern was observed around the circumference of the copper wire substrate (Figures 7, 8). Given the substantial oxygen evolution occurring under these conditions, the patterns bear substantial correspondence to gas bubbles spiralling around the wire.

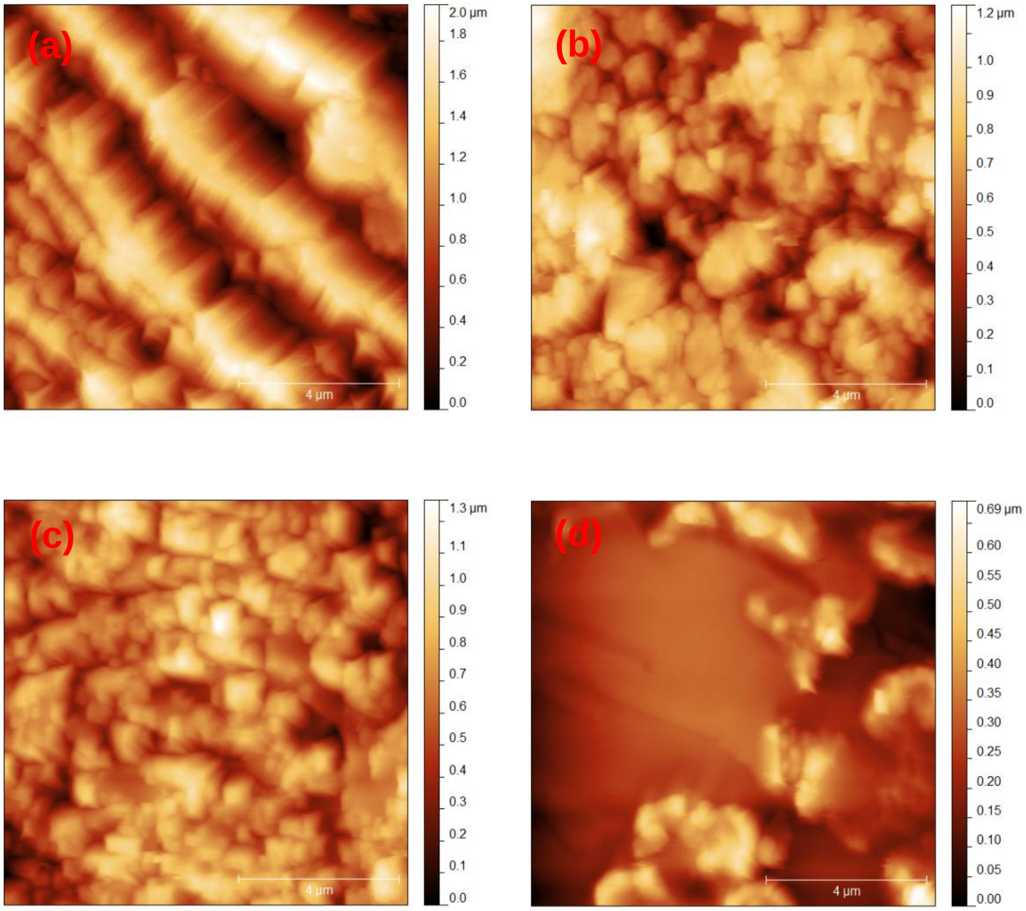

Figure 6: AFM images of vertical copper wire substrates anodized at 6V cell voltage for 8 min in 100% H_3PO_4 electrolyte at temperatures of 20^{o}C (a), 40^{o}C (b), 60^{o}C (c), 80^{o}C (d)

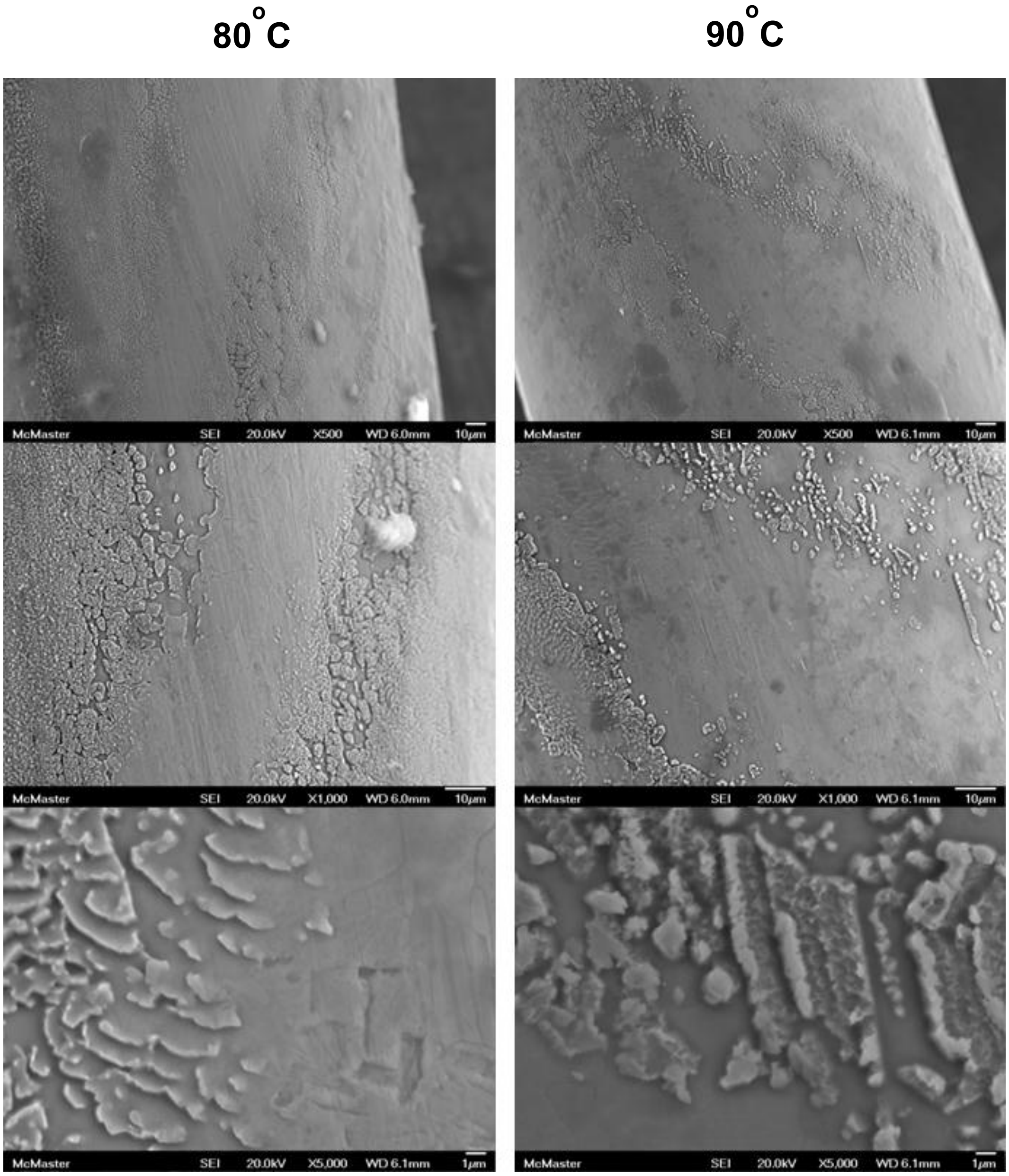

Figure 7: SEM images at 500X, 1000X, and 5000X magnification of vertical copper wire anodized in 100% H_3PO_4 at 80^{o}C and 90^{o}C for 8 min under an applied cell voltage of 6V

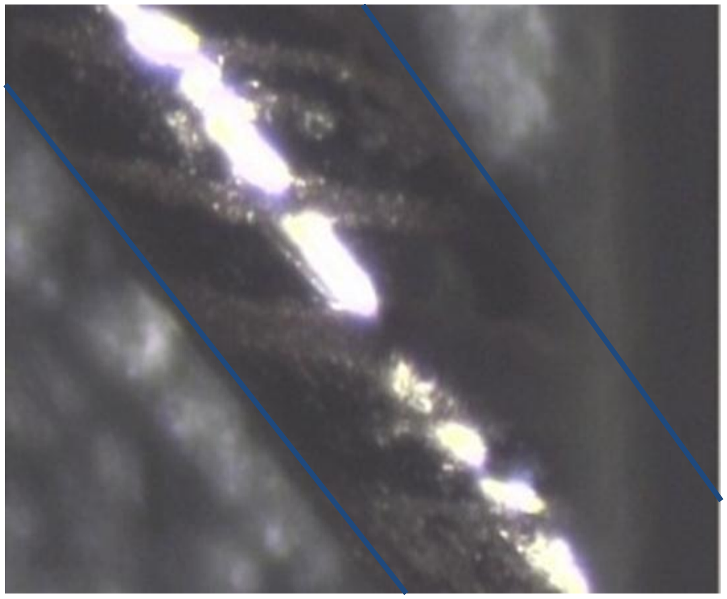

Figure 8: Optical image of vertical copper wire anodized in 100% H3PO4 at for 8 min under an applied cell voltage of 6V showing etched spiral pattern

3.2 – Potential Applications

Textured copper topography can lend itself towards application in surface enhanced Raman spectroscopy (SERS). Shown in figure 9 are two Raman spectra demonstrating the surface enhancement effect observed on the roughened copper surfaces. Figure 9(a) shows an enormous signal enhancement for a thin film of 100% H_3PO_4 on the etched copper substrate. All vibrational modes are significantly better resolved than in the bare copper case. This improvement in S/N ratio is further exemplified in figure 9(b) which shows the Raman spectra of stock orthophosphoric acid as a thin film on the etched copper substrate and the bulk liquid for comparison. The S/N ratio is comparable between the two but the surface enhanced signal shows a peak at approximately 720 cm^{-1}, characteristic P-O-P bending vibrations. This signal is thought to be caused by surface phosphoric acid dimerization. Nevertheless, the surface enhancement property of the etched copper substrate allows for their observation.

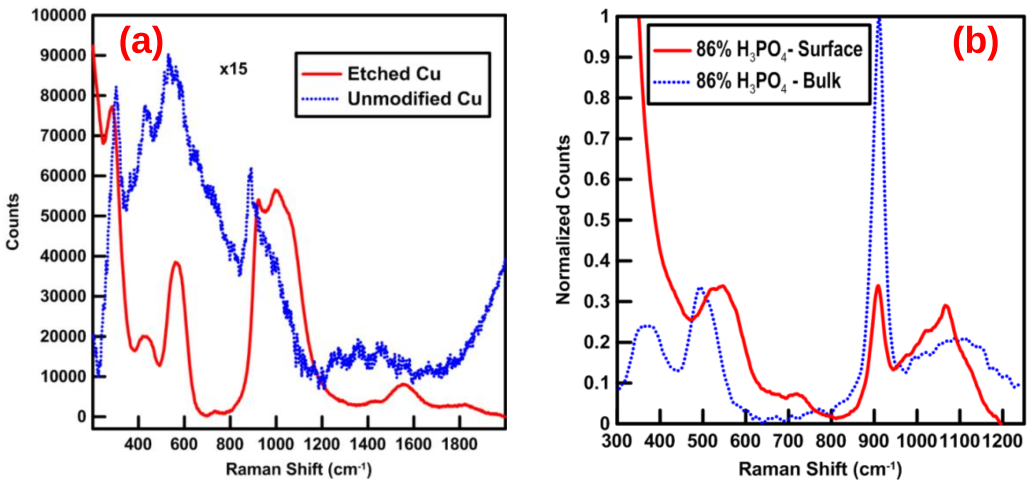

Figure 9: SERS activity of 100% H3PO4 on etched copper substrate (a) and observation of surface diphosphoric acid dimers on etched copper substrate (b)

The SERS active copper substrates were also tested for their applicability for use in electron field emission. This property is important in areas where electrons must be emitted into a vacuum and onto a sample substrate such as in field emission electron microscopy. Because the surface features were dissolved into the bulk substrate as opposed to deposited on a pre-existing surface, it was thought that the samples were more structurally sound. Structural integrity is a concern for current field emission substrates and can lead to the need for frequent replacement. To this end a preliminary study was conducted in collaboration with Dr. Ching's research group at McMaster University to observe any enhancement in field emission current. Their preliminary results are summarized in Figure 10.

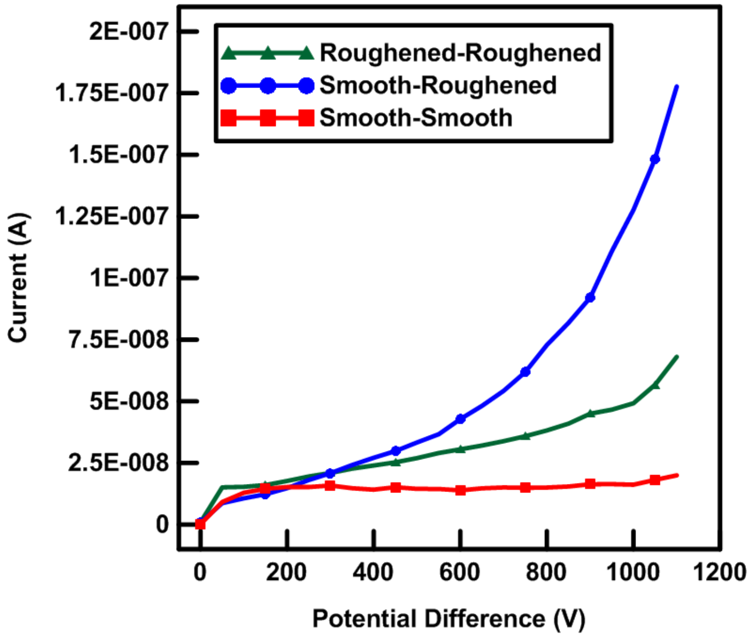

Figure 10: Evaluation of electron field emission performance for various combinations of smooth and roughened surfaces

It shows a clear increase in field emission current in when using the roughened copper substrates. While further research is currently being conducted towards this application it remains another possibility towards the utility of the roughened substrates.

3.3 – Mechanistic Study

A challenging aspect of investigating the previously described copper dulling under modified electropolishing conditions is the simultaneous copper dissolution and oxygen evolution. Many characterization tools are hindered either by the difficulty of separating the current contributions. Additionally, the physical presence of the bubbles makes spectroscopy difficult. Nevertheless a substantial array of different techniques was attempted where it was believed that in combination they might yield some valuable insight.

3.3.1 – Nuclear Magnetic Resonance (NMR) Spectroscopy

The high H_3PO_4 concentrations involved in the process of dulling copper can result in condensation of individual orthophosphoric acid units to produce dimers, trimers, and other more highly condensed oligomers. The use of ^{31}P NMR spectroscopy can elucidate the relative proportion of monomer, dimer, and trimer and thus was used to characterize bulk phosphoric acid electrolyte at three concentrations (Figure 11). It was observed that at concentrations corresponding to optical dulling there was a small amount of diphosphoric acid present. Its relative proportion was found to increase at higher H_3PO_4 concentrations. In addition the substantially higher viscosity involved contributed to an observed broadening of the associated peaks. However this doesn’t mean that the appearance of diphosphoric acid is causally related to the optical dulling observed. Further chemical characterization was conducted with the aid of XPS.

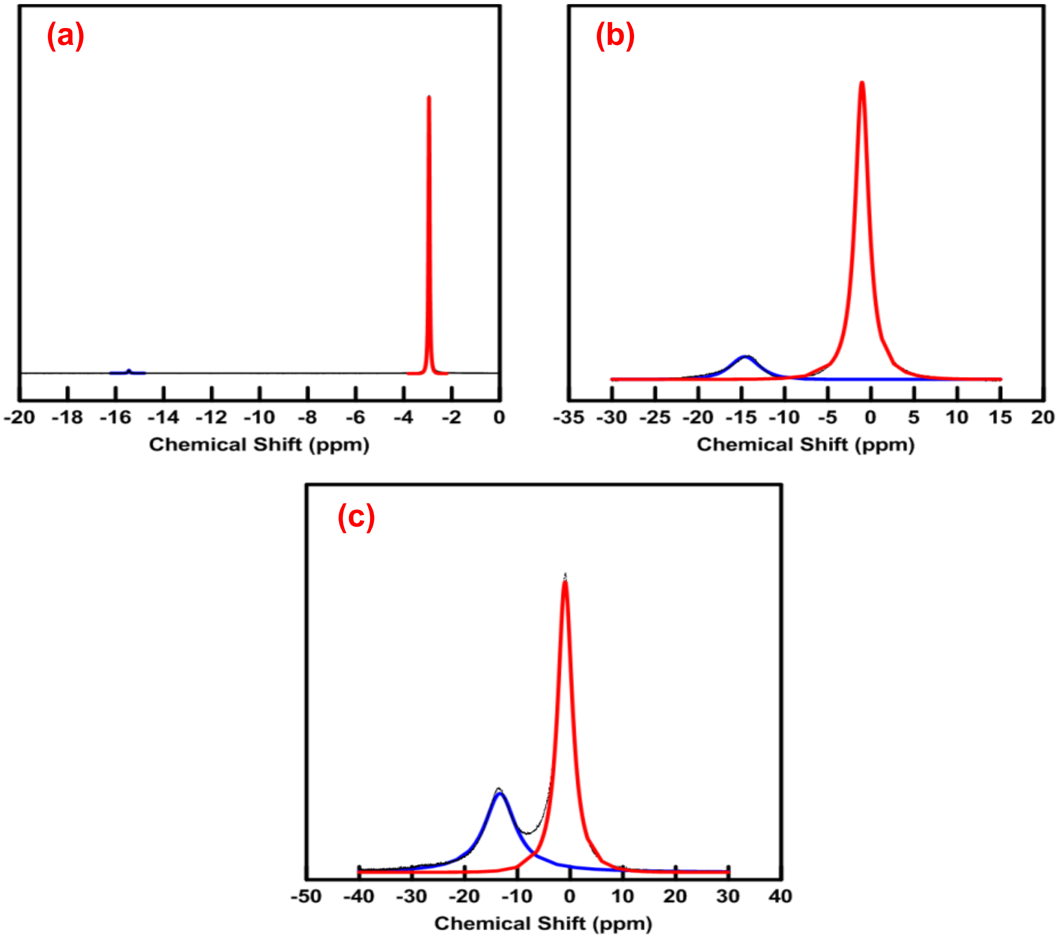

Figure 11: ^{31}P NMR spectra of pure phosphoric acid at 99% H_3PO_4 with 1 wt% diphosphoric acid (a), 102% H_3PO_4 with 13 wt% diphosphoric acid (b), and 104% H_3PO_4 with 28 wt% diphosphoric acid (c)

3.3.2 – X-ray Photoelectron Spectroscopy (XPS)

In an attempt to identify surface species present during anodization XPS was performed on a sample of copper that had been anodized in 100% H_3PO_4 and subsequently frozen in liquid nitrogen. While remaining under liquid nitrogen, the sample was transferred into an appropriately cooled XPS spectrometer with a thin layer of frozen phosphoric acid still left on the sample. Such a method represented the easiest way available of approximating an in-situ experiment, but it also left the sample with an uneven distribution of phosphoric acid. Figure 12 details the copper XPS spectrum of the near surface phosphoric acid electrolyte. While the time used to collect the spectrum was insufficient to generate peaks that could be reliably fitted, it does still indicate the presence of Cu^{2+}. This is confirmed by the shakeup peak at approximately 943 eV which is a loss process independent of copper XPS and Auger lines and is only found in the presence of Cu^{2+}.[52] Further XPS performed on a sample with view of the bare copper surface only conclusively showed the presence of metallic copper and Cu^{2+} (Figure 13). Again however the signal to noise ratio was insufficient to perform a proper peak fitting analysis. High resolution XPS analysis was also performed at O 1s and P 2p binding energies (Figures 14 and 15). Unfortunately the results obtained were inconclusive as the resultant peak fittings only corresponded to the expected spectrum for frozen phosphoric acid.

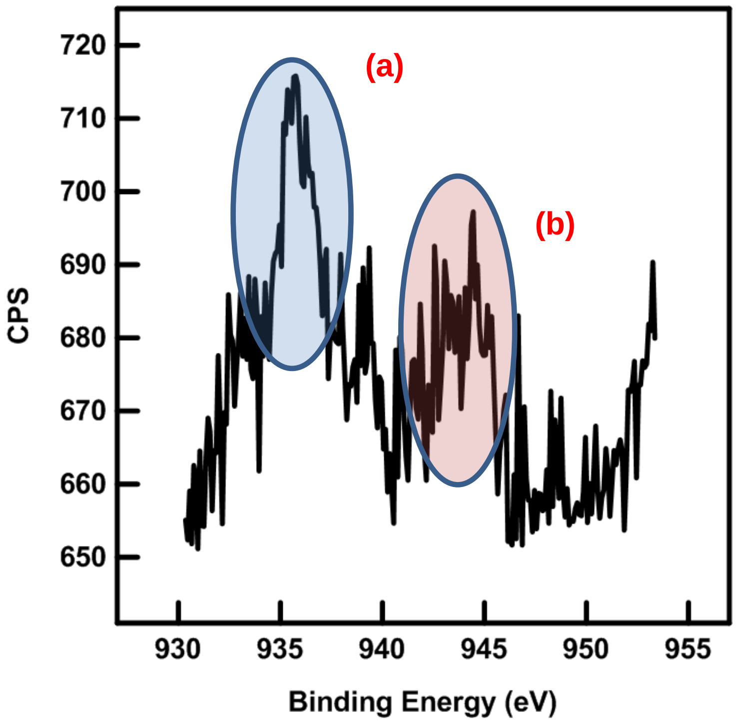

Figure 12: Copper XPS spectrum of near surface phosphoric acid electrolyte with no view of bare copper anode showing the Cu $2p^{3/2}$ photoelectron loss at ~ 935 eV indicative of Cu^{2+} (a), as well as the presence of a shake up peak confirming the presence of Cu^{2+} (b)

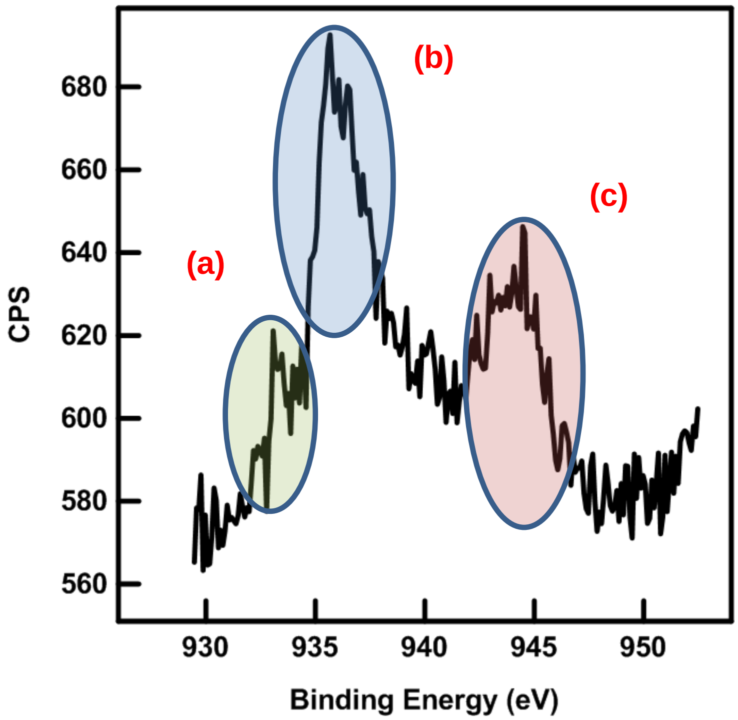

Figure 13: Copper XPS Spectrum of near surface phosphoric acid electrolyte with view of bare copper anode showing the Cu $2p^{3/2}$ photoelectron loss at ~ 933 an 935 eV indicative of Cu^0 (a) and Cu^{2+} (b) respectively

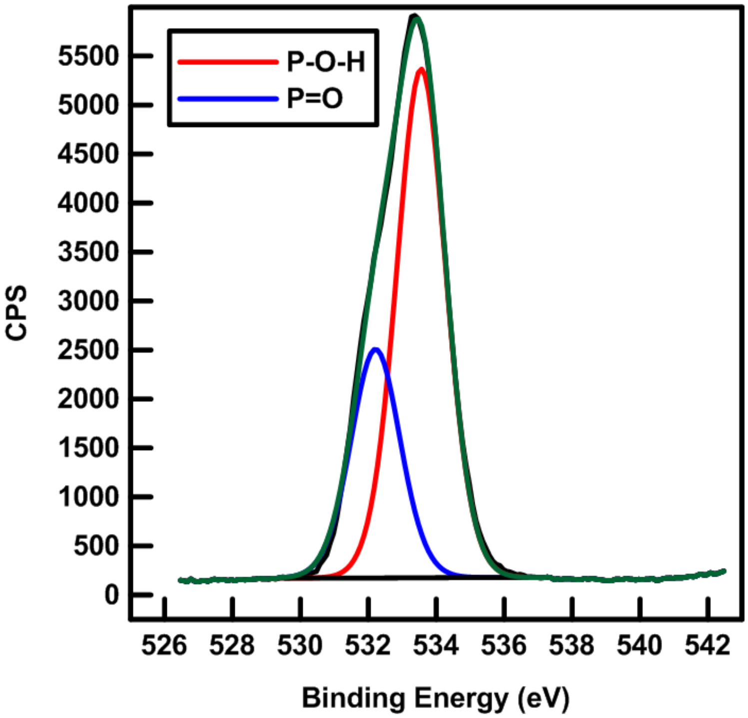

Figure 14: Oxygen XPS spectrum of near surface phosphoric acid electrolyte with view of bare copper anode showing the photoelectron loss peaks associated with oxygen 1s for both the protonated and doubly bonded oxygen.

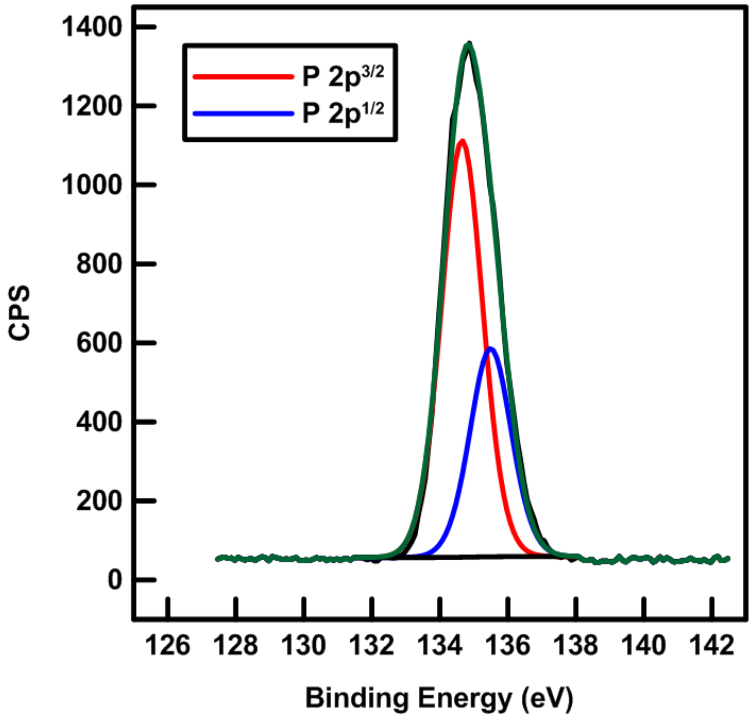

Figure 15: Phosphorous XPS spectrum of near surface phosphoric acid electrolyte with view of bare copper anode showing the photoelectron loss peaks associated with phosphorous 2p for both the 3/2 and 1/2 states.

3.3.3 – Spectroscopic Ellipsometry

Attempts were made to conduct in-situ spectroscopic ellipsometry during anodization. This would have the advantage of being able to discern physical properties of the near surface layer including thickness and any potential heterogeneity as signified by variations in refractive index. Monitoring was to be performed over a range of applied potential potentials and H_3PO_4 concentrations. Referencing this information to the time elapsed would further understanding of the time dependent system properties. Unfortunately various complications were encountered which made such an analysis unfeasible.

Initial experiments involved an open setup with the phosphoric acid electrolyte exposed to the air. Even before application of bubble generating potentials a small degree of instability was present at the phosphoric acid/air interface. This yields a changing, uneven surface to the incident polarized light. As spectroscopic ellipsometry is dependent on specular reflection the inherent instability was sufficient to remove the specular reflectance condition and make reliable measurements impossible. Properly designed liquid cells exist which are completely filled with the desired liquid, eliminating the variable electrolyte/air interface. However because the dulling conditions occur in areas where oxygen bubbles are generated, it is likely that this would interfere with specular reflectance to an even greater degree. Consequently it was determined that spectroscopic ellipsometry was unlikely to work under the relevant conditions.

3.3.4 – In-situ Raman Spectroscopy

While the SERS effect had already been demonstrated on the roughened copper substrates, it was thought that it might also yield information on potential chemical changes occurring during anodization. To this end Raman spectroscopy was performed on a copper sample before and during the application of an applied potential (Figure 16).

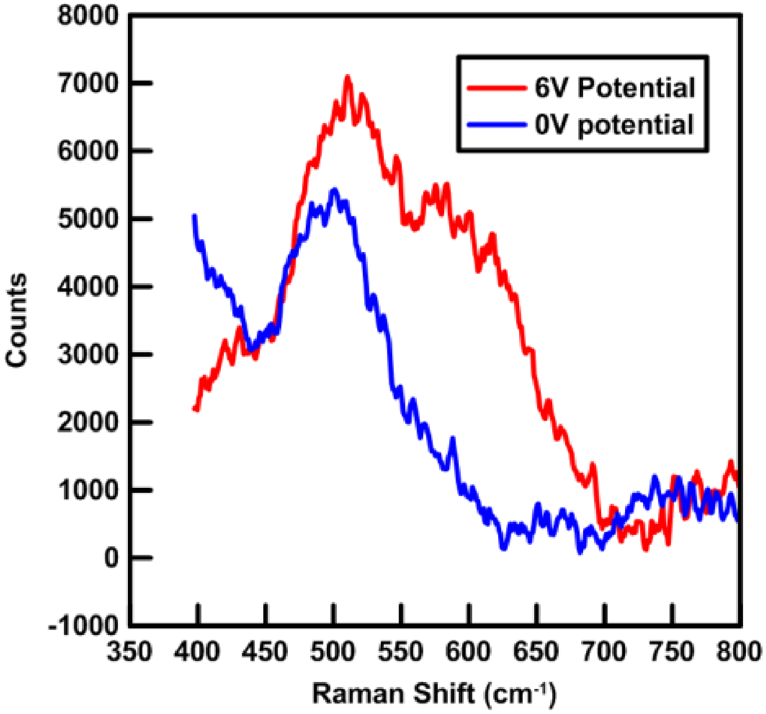

Figure 16: In-Situ Raman spectrum of copper substrate immersed in 100% H_3PO_4 before and during the application of a 6V potential difference

The only area of the spectrum that exhibited change was where copper oxide species are typically found. While there was a small change upon application of a 6V potential that might be indicative of the appearance of Cu^{2+} such an observation was neither informative nor surprising. As such, other in-situ methodologies were attempted to probe the system in further detail.

3.3.5 – Electrochemical Impedance Spectroscopy

The goal of EIS was to identify and interpret an impedance signature characteristic of the onset of dulling conditions. Depicted in figure 17 is a Nyquist plot of a representative experiment conducted with 99% H_3PO_4 electrolyte. The capacitive semicircle observed is characteristic of the impedance behaviour charge transfer at the anode. By measuring the radius of the semicircle the anode charge transfer resistance can be determined. Immediately clear is the deviation from a strict linear trend. While the radius initially increases a dramatic drop is observed at approximately 3V followed by the continuation of the steady increase. This behaviour coincides with the appearance of an inductive loop which is indicative of simultaneously occurring oxygen evolution.

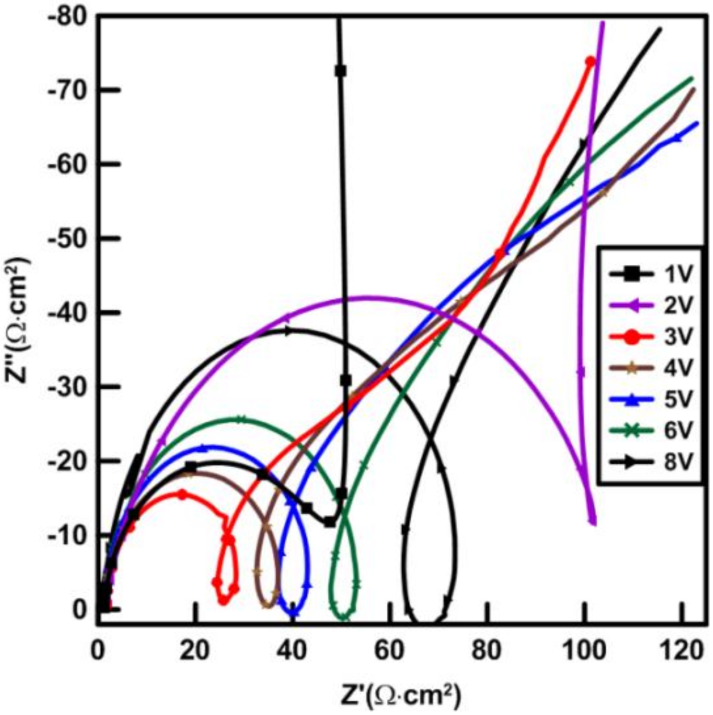

Figure 17: High frequency portion Nyquist plot of vertical copper wire at 20°C in 99% H_3PO_4 with variable applied potential versus SCE

EIS measurements were expanded across several concentrations and the corresponding charge transfer resistances were measured (Figure 18). Charge transfer minima were observed for low H_3PO_4 concentrations. The charge transfer minimum showed a subtle shift towards higher potentials. The highest H_3PO_4 concentrations did not show a minimum but rather a resistance plateau was observed at higher potentials. The charge transfer minimum alone is insufficient to indicate optical dulling. This is evidenced by the absence of dulling under regular conditions in 86 and 93% H_3PO_4.

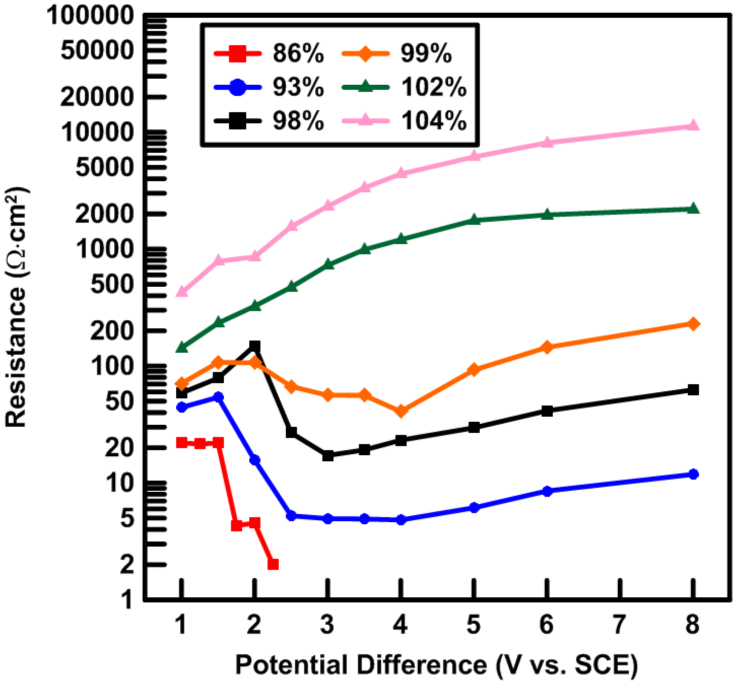

Figure 18: Charge transfer resistance of vertical copper wire at 20°C measured from width of capacitive semicircle with variable voltage and H_3PO_4 concentration

Nevertheless, it hints to the importance of convection as caused by vigorous oxygen evolution. Specifically, because of the high viscosities and low mass transfer rates found under these conditions the charge transfer resistance can be significantly reduced through convective mixing. The evolving bubbles increase mass transfer rates at the anode thereby lowering the charge transfer resistance. This would also explain the behaviour at high H_3PO_4 concentration where the limited water content is not conducive to promoting oxygen bubble based convective mixing.

3.3.6 – Viscosity and Oxygen Evolution

The results of the EIS measurements merited further investigation into the effect that oxygen bubbles have on the system. An important characteristic noted under optical dulling conditions is the increased difficulty with which bubbles detach from the anode. Shadowing by stationary, long-lived bubbles could explain the resultant topography. The higher viscosity at these conditions was believed to promote such bubble behaviour. As detailed in figure 19 there is a sharp upward trend for viscosity past 98% H_3PO_4. Values for kinematic viscosity under optical dulling conditions are approximately triple that for 86% H_3PO_4. As a point of comparison, the kinematic viscosity for water is approximately 1 cS at room temperature[53], two orders of magnitude lower than the 100% H_3PO_4 value.

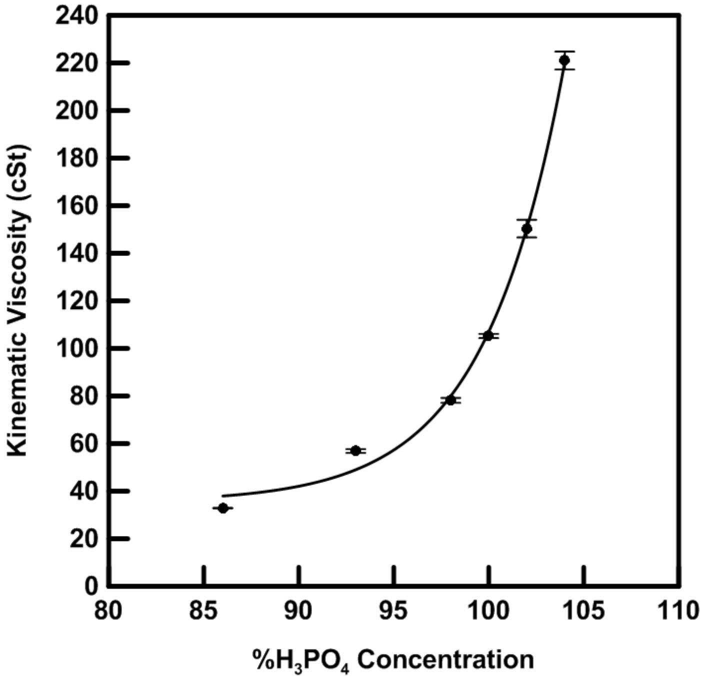

Figure 19: Kinematic viscosity of various H3PO4 concentrations at 20^{o}C

As expected viscosity is also variable with temperature (Figure 20) and has implications for the optical dulling temperature dependence. The observed viscosity decrease might be responsible for changing various viscosity dependent parameters including bubble behaviour. Unfortunately, as described previously, the system does not lend itself to simple variable separation. Also there was some random variability in the replicates used to collect each data point. This resulted in the relatively small confidence intervals at a 95% confidence level.

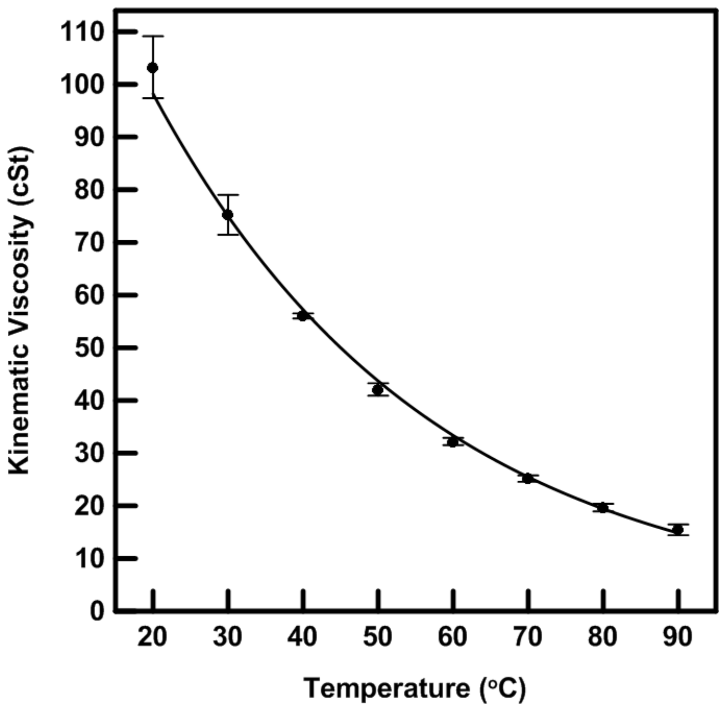

Figure 20: Kinematic viscosity of 100% H_3PO_4 at various temperatures

It is important to note however that as phosphoric acid concentration and viscosity increase, overall water content decreases. Correspondingly the oxygen evolution rate also tends to decrease. Oxygen collection experiments were conducted to indirectly investigate this decrease as indicated by the oxygen evolution current density. Though there was substantial variability concerning measurements at low oxygen evolution rate as dictated by the lowest measurable volume on the graduated syringe. Shown in figure 21 are the current contributions of both water dissociation and copper dissolution. It is clear that oxygen evolution is responsible for the majority of the current during dissolution for all but the most highly concentrated phosphoric acid solutions. At 104%

H_3PO_4 the volume of evolved oxygen was low enough so as to not be measureable.

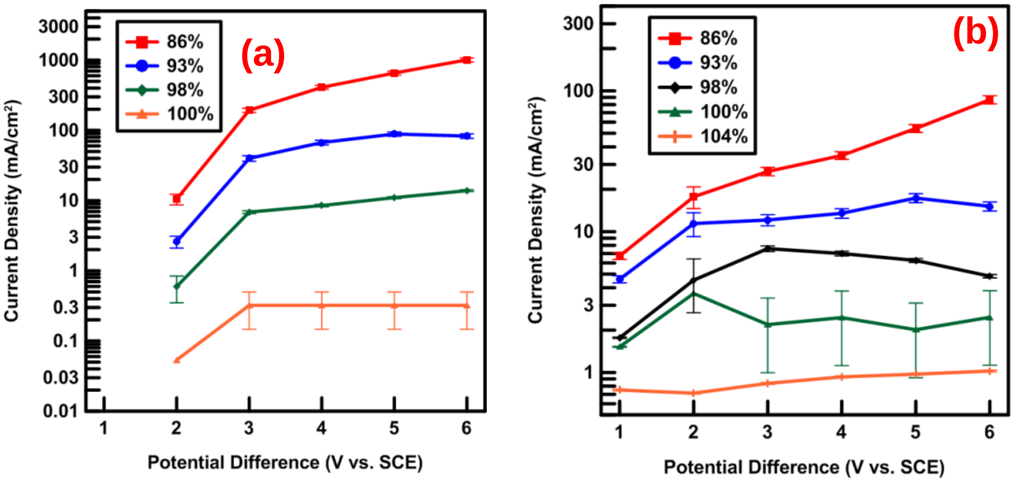

Figure 21: Oxygen evolution current density with variable voltage (a) and the corresponding copper dissolution current density (b)

An interesting comparison can be made between the current density distribution at 93 and 98% H_3PO_4. The copper dissolution current density at 98% H_3PO_4 is within 50% of the value at 93% H_3PO_4 after 3V. However the difference in water dissociation current density is significantly larger at only 10% of the value at 93% H_3PO_4. Optical dulling is not typically observed with 93% H_3PO_4 but always observed with 98% H_3PO_4. Comparing the ratio of the two currents (Figure 22) shows a plateau for the lower concentrations with a breakdown of this behaviour occurring in the dulling regime.

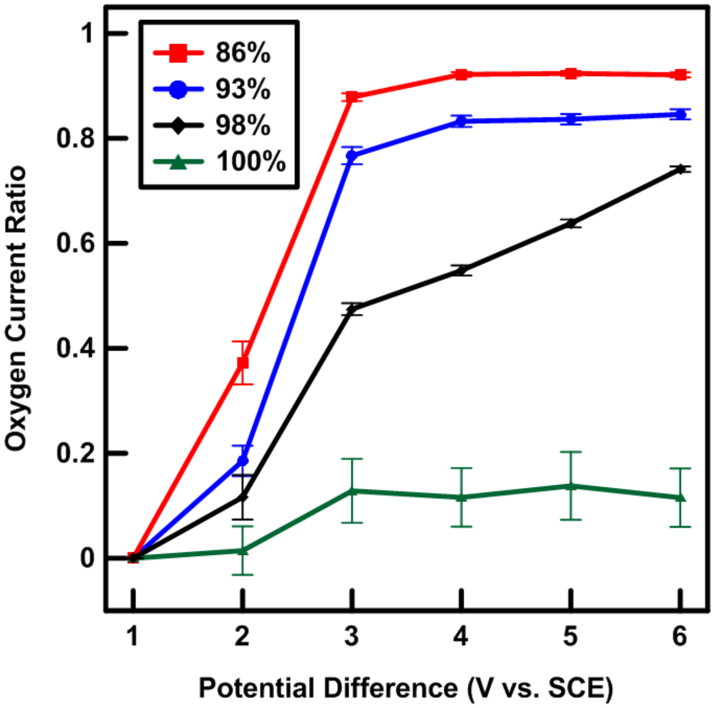

Figure 22: Fractional proportion of current density between oxygen evolution and copper dissolution

Anecdotal evidence had shown that the optical dullness would appear and then slowly disappear under extended anodization conditions. This condition is exemplified in Figure 23. A trend is observed where the initial rough topography which gives rise to the optical dulling is slowly removed as anodization is allowed to continue. Given this observation, time resolved oxygen evolution data was collected to help explain the disappearance of surface roughness (Figure 24). In stagnant electrolyte the copper dissolution current stays relatively constant where the oxygen evolution current drops precipitously. With application of pre-stirring the current behaviour changes dramatically. Notably, the initial current with stirring is higher than encountered for the first data point in the non-stirred experiments. This could be explained by an increased Cu^{2+} concentration enhanced electrical conductivity in the viscous medium or potential hydrolysis with atmospheric water vapour. In either case, stirring before each trial promotes more stable, plateau-like behaviour.

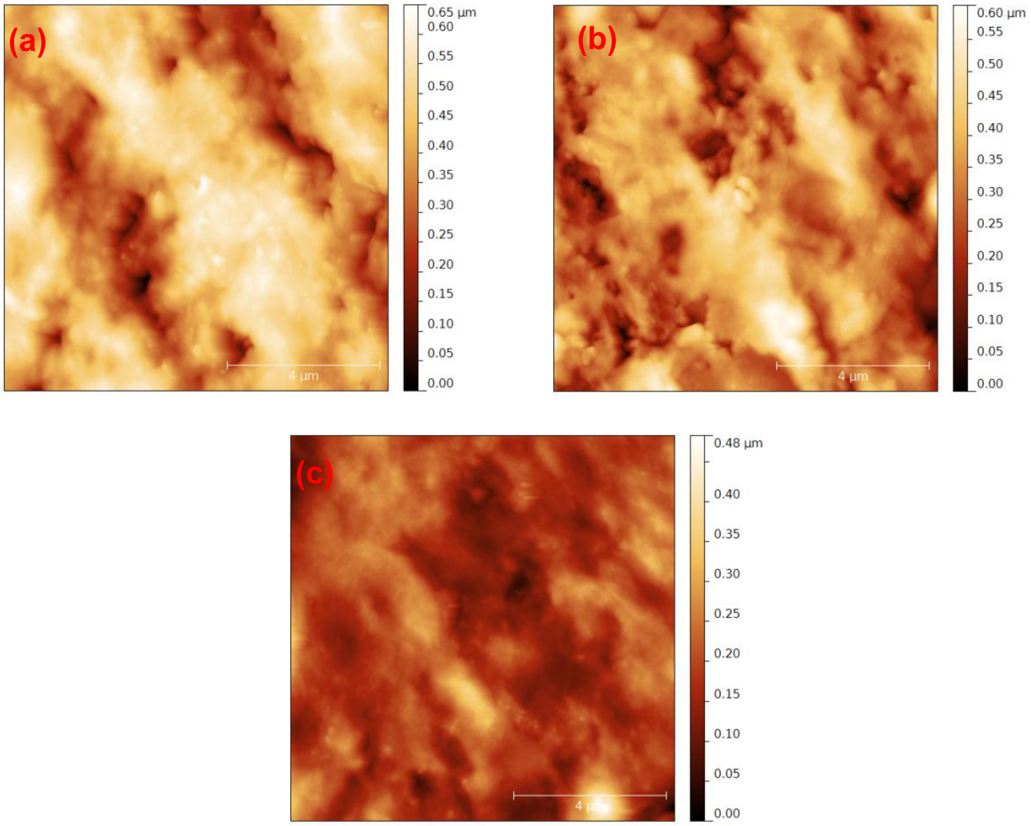

Figure 23: AFM images of copper wire substrate anodized in 99% H_3PO_4 at 20^oC without stirring for 8 min (a), 15 min (b), and 30 min (c)

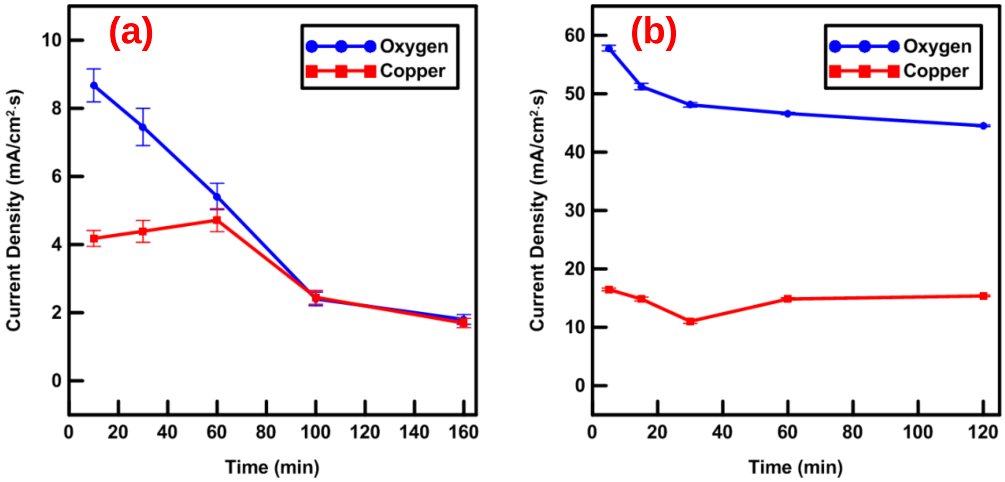

Figure 24: Current contributions of both oxygen evolution and copper dissolution in 99% H_3PO_4 at 20^{o}C conducted without stirring between data points (a) and with 30 min of pre-stirring before each data point (b)

3.3.7 – Substrate Orientation

In an effort to isolate all other variables except for bubble induced effects, flat copper surfaces were anodized in phosphoric acid of varying concentration and at different orientation. As buoyancy is the driving force behind bubble ascension, changing the substrate orientation only influences bubble dynamics and does not directly affect other aspects of the anodization. Figure 25 demonstrates the relative flatness observed with anodization of a vertical copper substrate in 93% H_3PO_4 at a 6V cell potential. Upon changing the orientation to horizontal facing downwards there is a marked surface roughening observed.

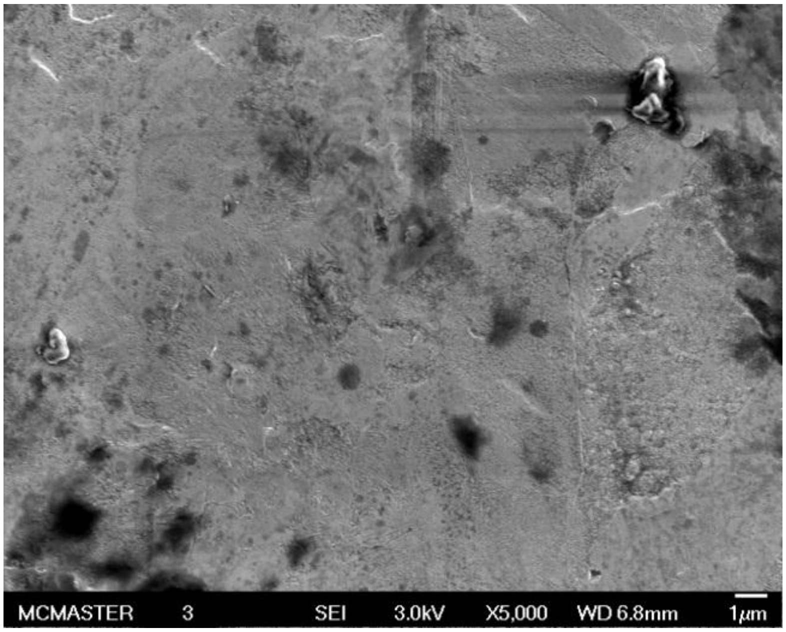

Figure 25: SEM image of planar copper sheet anodized at 40^{o}C, in 93% H3PO4 at a 6V cell voltage for 8 min in a vertical orientation

From a macroscopic perspective the surface displayed the characteristic optical dulling of a roughened surface. This was further supported through SEM imaging (Figure 26). While the etch pattern appears more disorderly than those obtained at higher H_3PO_4 concentrations there is a clear orientation dependence.

Orientation plays a role under typical etching conditions as well. Figure 27 shows two etched samples in horizontal facing down and vertical orientations Flat plateaus have developed on the horizontal sample but are absent in the vertical sample. Additionally, the horizontal sample shows a lower degree of uniformity over the vertical sample. While the changes are certainly subtler than that observed at 93% H_3PO_4 there still exists an orientation dependence.

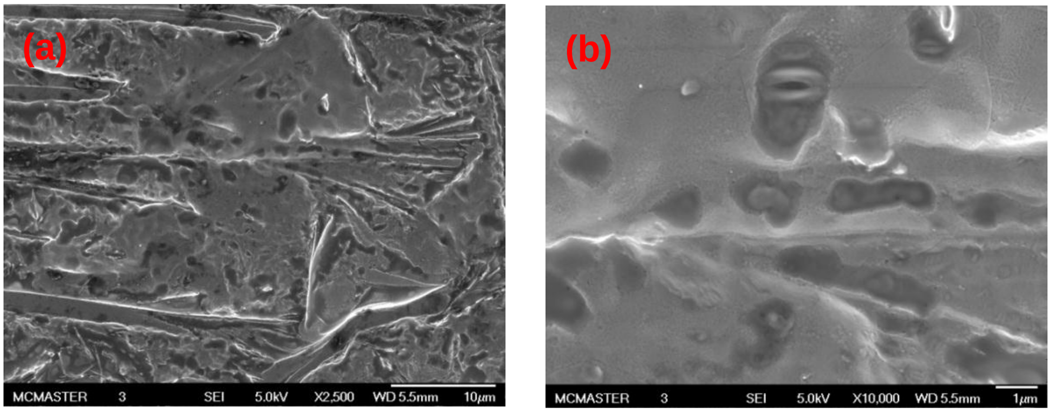

Figure 26: Copper sheets anodized in 40^{o}C, 93% H3PO4 at a 6V cell voltage for 8 min in a horizontal facing down geometry at 2,500X (a) and 10,000X (b) magnification

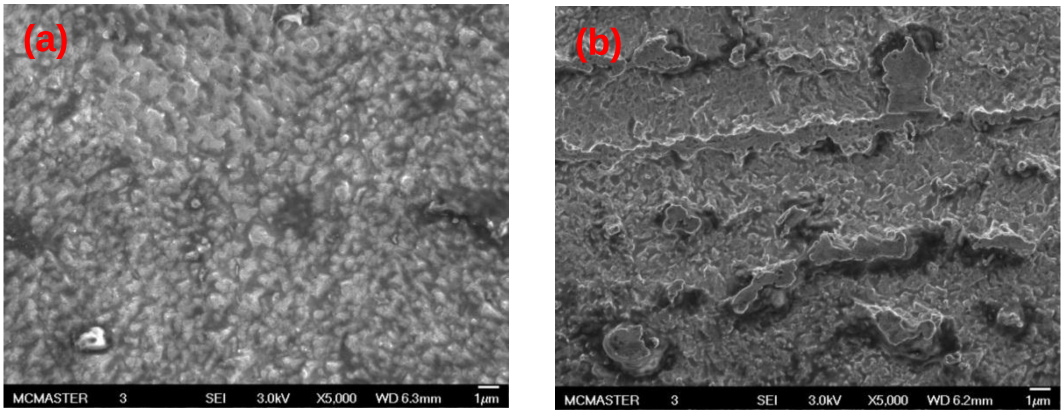

Figure 27: Copper sheets anodized in 40^{o}C, 100% H3PO4 at a 6V cell voltage for 8 min in vertical (a) and horizontal facing down (b) orientations

In addendum to these experiments a test was conducted to determine whether oxygen gas specifically was necessary to cause optical dulling. Hydrogen gas was collected on the underside of a horizontal facing downwards anode. A potential below the oxygen evolution potential was applied in the presence of a trapped hydrogen bubble. Figure 28 depicts the results where an etching effect is clearly observed in comparison to unmodified copper. While the conditions are not strictly comparable given the static nature of the experiment, it contributes further to the idea that the simple presence of a gas in close proximity to the electrode can result optical dulling.

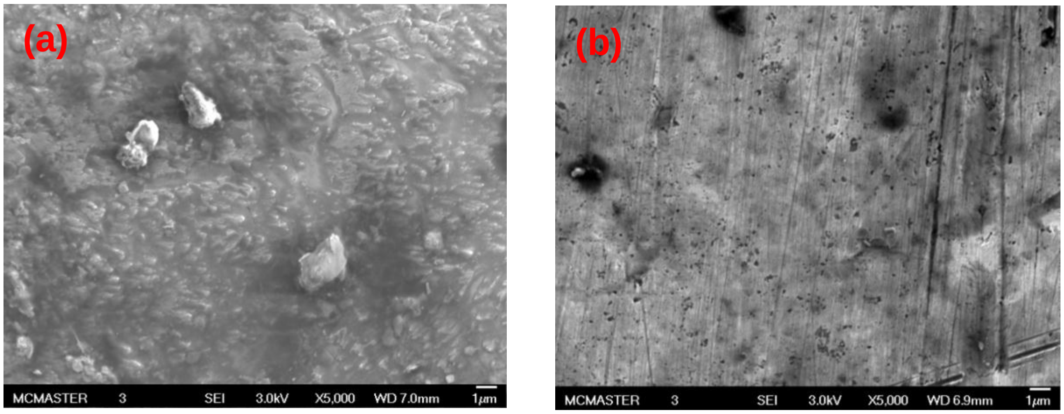

Figure 28: Copper sheets anodized in 40^{o}C, 93% H3PO4 at a 1.5V cell voltage for 30 min with trapped large hydrogen bubble in hemispherical, horizontal facing downwards depression (a) in comparison to bare unmodified copper (b)

3.3.8 – High Speed Optical Microscopy

Given the apparent influence of bubble formation on surface topography attempts were made to better visualize their formation. Unfortunately as bubbles detach they tend to persist for long periods of time in the near surface volume. This obscures the view of the surface and other newly forming bubbles. For lower H_3PO_4 concentrations complete surface obscuration can occur within a fraction of a second. Thus, a high speed camera serves well for capturing images in the small window of time available for useful imaging.

To start anodization of a copper substrate in 93% phosphoric acid was performed (Figure 29). After only a tenth of a second substantial gas evolution is observed, and after 1 full second the surface view completely obscured by rising gas bubbles unattached to the surface. This is shown in direct comparison to 98% H_3PO_4 (Figure 30). It was observed that at 1 second after the beginning of anodization there were smaller and more numerous bubbles in 98% H_3PO_4 as compared to 93%. Given the higher viscosity and lower oxygen evolution rate associated with 98% phosphoric acid the result is unsurprising. Nevertheless the persistence of smaller bubbles closer to the surface for an extended length of time may help explain how dulling was not observed at 93% H_3PO_4 but is seen at 98%. Further imaging was performed with anodization in 100% H_3PO_4 with substantially different behaviour being observed (Figure 31). Specifically, even after 10 seconds there are still unhindered views of the surface. These views show bubbles at various points above the surface along with their corresponding size variation.

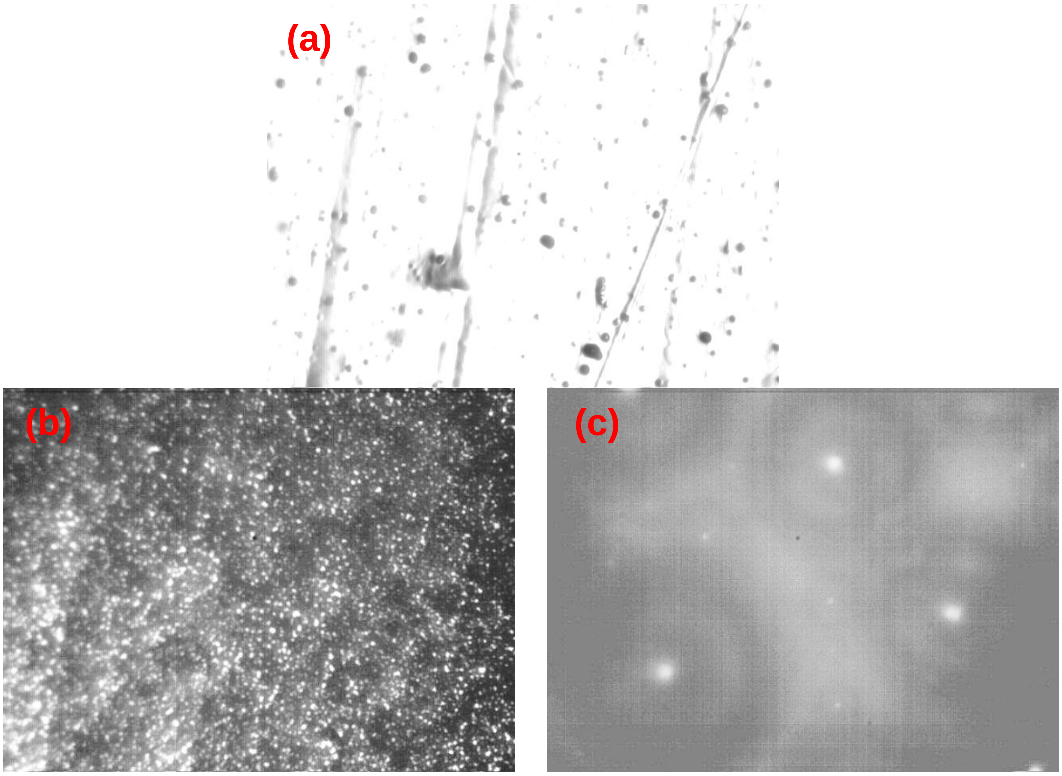

Figure 29: Still image snapshots (400 µm across) of high speed camera optical microscopy showing the initial unanodized copper substrate immersed in 93% H_3PO_4 (a), the resultant bubble pattern observed after anodization under a 6V cell potential after 0.1s (b), and after 1s (c)

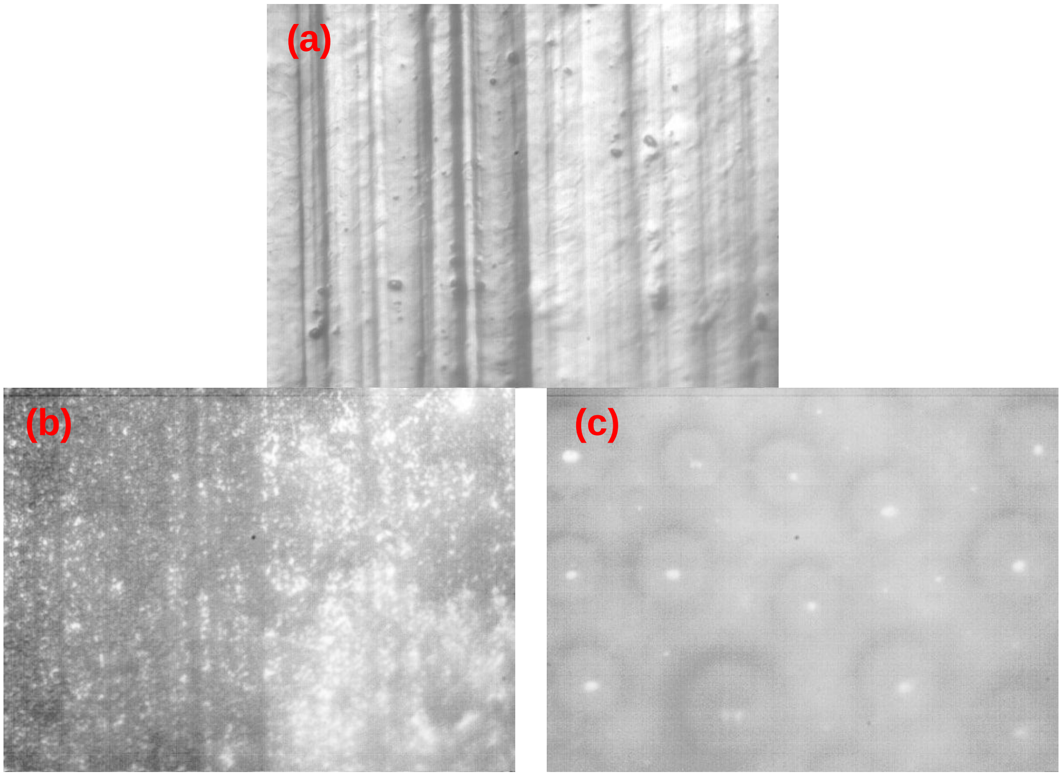

Figure 30: Still image snapshots (400 µm across) of high speed camera optical microscopy showing the initial unanodized copper substrate immersed in 98% H_3PO_4 (a), the resultant bubble pattern observed after anodization under a 6V cell potential after 0.1s (b), and after 1s (c)

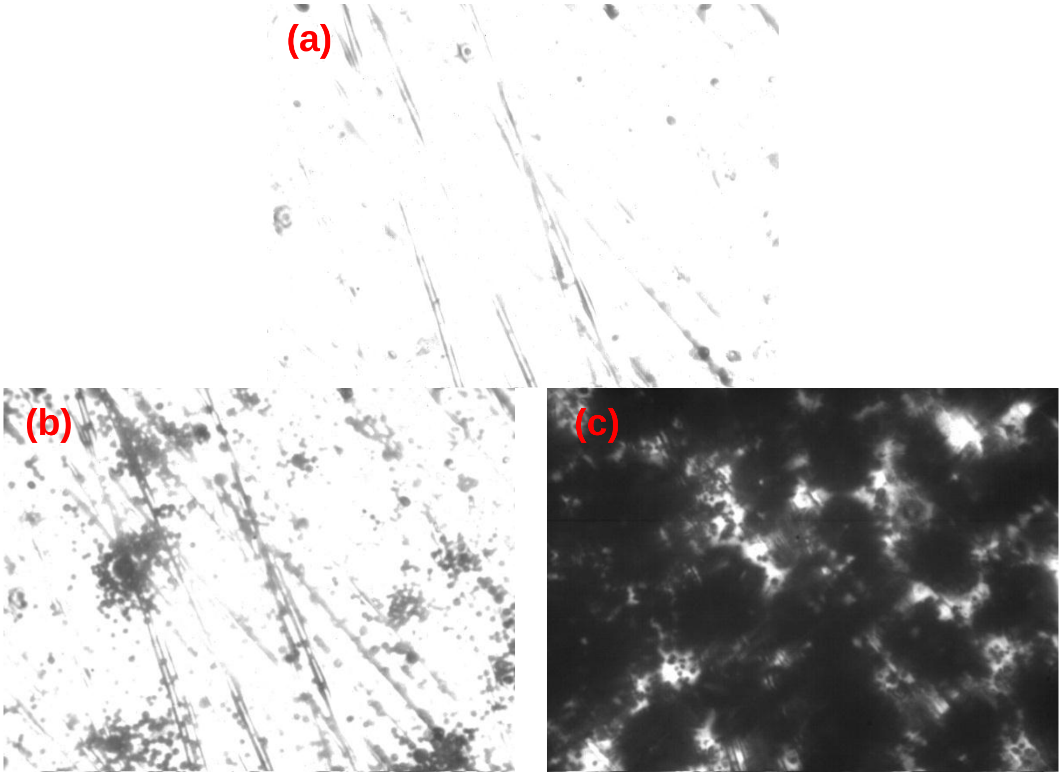

Figure 31: Still image snapshots (400 µm across) of high speed camera optical microscopy showing the initial unanodized copper substrate immersed in 100% H_3PO_4 (a), the resultant bubble pattern observed after anodization under a 6V cell potential after 1s (b), and after 10s (c)

Chapter 4: Discussion, Conclusion, and Future Directions

4.1 – Discussion

Interpretation of the results can be conducted from both practical and mechanistic standpoints. From the practical perspective it has been shown that deviations from typical copper electropolishing conditions can lead to potentially useful surface topography. Feature heights range from 0.5-2 micron and can yield surface area increases upwards of 30% over unmodified copper. They have been shown to function as SERS substrates and have even exhibited positive results on preliminary studies towards their use in electron field emission.

Another interesting aspect of this phenomenon includes the many degrees of freedom with which it can be manipulated. Various parameters play a role in the kind of topography obtained e.g. temperature, H_3PO_4 concentration, orientation, and geometry. While this impacts reproducibility it is nevertheless well suited to substantial optimization towards specific applications. This could potentially involve using the generated topography as a template for finer modification.

While there is substantial room for optimization, the optical dulling mechanism is less clear. The dynamic thin film nature of the system makes it difficult to characterize. Adding to this the presence of vigorous oxygen evolution one can exclude a substantial fraction of currently available instrumentation. Another difficulty is the substantial variable coupling, where changing one variable simultaneously changes multiple others making it difficult to isolate casual relationships. Nevertheless, much of the data collected thus far indicates oxygen evolution behaviour being a driving force behind the dulled surfaces.

In a vertical geometry the only condition under which dulling occurs spontaneously are when the voltage versus SCE exceeds 3V and the phosphoric acid concentration is between 98 and 100% H_3PO_4 at room temperature. It is clear that the mere presence of oxygen evolution is not sufficient. Oxygen evolution begins at 2V versus SCE and no dulling is observed at that potential even with a suitable H_3PO_4 concentration. Also it is believed that the same chemical species present at 2V are also present at higher potentials. In-situ Raman spectroscopy, NMR spectroscopy of bulk phosphoric acid, and x-ray photoelectron spectroscopy (XPS) of suitably frozen samples were unable to detect the presence of anything other than Cu^{2+}, water, orthophosphoric and diphosphoric acid in the near surface electrolyte. While this does not completely rule out a novel chemical explanation it does detract from its validity.

The 98-100% concentration range represents an optimum point with respect to viscosity and water content. Higher concentrations are relatively uninteresting as the limited water concentration and high viscosity is insufficient to yield significant dissolution. At lower concentrations however the electrolyte is substantially less viscous and possesses greater water content. The rate of dissolution and oxygen evolution is thus proportionally higher than in the more concentrated scenarios. Observation of the anode under these conditions shows a rapid and vigorous release of large bubbles which generate substantial bulk electrolyte convection akin to mechanical stirring. Etching is only observed under these conditions if the anode is placed in a horizontal facing downwards orientation.

An important point about the orientation experiment is that the only aspect of the system that could have geometry dependence is the buoyancy force acting on the bubbles. The fact that dulling was turned on and off in a usually non-dulling regime with a mere change in substrate orientation puts strong emphasis on the importance of oxygen evolution. It also helps to exclude other theories involving a substantial difference in the chemical environment at higher H_3PO_4 concentration.

These results raise the question of the specific role of bubbles in the development of the observed surface topography. It is clear that bubbles both inhibit dissolution current by insulating the surface from the electrolyte, and promote it by generating convective currents as they accelerate through the electrolyte under their own buoyancy. However, both the bubble trapping experiments at low H_3PO_4 concentration and the optimal conditions at high H_3PO_4 concentration inhibit bubble departure from the electrode. While this was done physically in the former, this was achieved in the latter by virtue of the limited water content restricting the oxygen evolution rate and retarding bubble ascension through viscous resistance. The indication is that increasing the departure time of electrolytically evolved bubbles is important to generating the observed surface topography. The data taken collectively enable the proposal of mechanisms for copper dulling based on bubble behaviour.

Oxygen gas dissociated electrolytically supersaturates the near electrode area and forms bubbles at nucleation sites located in depressions. At sufficiently high potential and H_3PO_4 concentration the bubbles form relatively slowly, stay small in size, and do not depart the surface easily. The persistent surface bubbles mask the electrode area beneath them and prevent dissolution. If the bubbles persist long enough, unprotected areas will dissolve to a point substantially beneath the height of the originally protected depression. As the bubbles depart, the newly formed depressions begin to serve as nucleation sites and the cycle begins anew. Given sufficiently small bubbles one can generate the small length scales observed in the SEM and AFM images of the etched substrates and explain the semi-ordered patterns thus observed.

Another proposal is the effect of a high bubble density in the vicinity immediately above the electrode within the viscous layer. The gaps in-between the bubbles could serve as channels by which dissolution could occur. As this layer is constantly changing the surface pattern it dictates would also change. The overall decrease in charge transfer resistance could be maintained as the convective effect of the rising gas would outweigh the microscale masking effect.

These proposals are somewhat at odds with the conditions which occur during dimple formation. The gas evolution behaviour is substantially less pronounced when comparing dimple formation to copper etching. Dimples are also more ordered and have far smaller dimensions then their copper counterparts. The differences are too great to draw a clear link between the two and it is likely that they occur by two separate mechanisms. While this doesn't rule out the influence of gas evolution during dimple formation[54] it likely doesn't impact topography in the same way that gas evolution on copper does.

4.2 – Summary and Future Directions

This thesis has outlined the basic characteristics of an etching phenomenon observed on copper substrates anodized in phosphoric acid. It was observed that it can yield semi-ordered patterns with micron scale topographic features. Importantly this was achieved under conditions more closely related to electropolishing conditions. This transition is believed to be closely related to oxygen evolution and specifically the resultant bubble dynamics. It is thought that the highly viscous yet electrically conductive conditions keep substantial bubble density closer to the surface for an extended period of time. This promotes an anisotropic current regime dictated by the bubbles and supersedes other dissolution regimes occurring simultaneously. It is believed that copper etching under the aforementioned conditions has not been previously reported in literature.

Further research on the topic from an application based perspective would involve evaluating the substrate performance towards various uses. Because the features are etched in rather than deposited they possess greater structural integrity and are more suited to rigorous environments. They also possess the potential for post-modification as is necessary for the application. Mechanistically, a demonstration of the phenomenon in separate system would confirm the validity of the proposed explanation. This could be achieved by considering another electropolishing system such as that based on sulphuric acid. Various parameters including temperature or orientation could be varied to achieve a similar effect to that observed with copper and phosphoric acid.

5.1 – References

(1) Ruibal, R.; Ernst, V. The structure of the digital setae of lizards. *Journal of Morphology* **1965**, *117*, 271–293.

(2) Irschick, D. J.; Austin, C. C.; Petren, K.; Fisher, R. N.; Losos, J. B.; Ellers, O. A comparative analysis of clinging ability among pad-bearing lizards. *Biological Journal of the Linnean Society* **1996**, *59*, 21–35.

(3) Pugno, N. M. Spiderman gloves. *Nano Today* **2008**, *3*, 35–41.

(4) Schiff, L. I. Possible New Experimental Test of General Relativity Theory. *Phys. Rev. Lett.* **1960**, *4*, 215–217.

(5) Everitt, C. W. F.; DeBra, D. B.; Parkinson, B. W.; Turneaure, J. P.; Conklin, J. W.; Heifetz, M. I.; Keiser, G. M.; Silbergleit, A. S.; Holmes, T.; Kolodziejczak, J.; Al-Meshari, M.; Mester, J. C.; Muhlfelder, B.; Solomonik, V. G.; Stahl, K.; Worden, P. W.; Bencze, W.; Buchman, S.; Clarke, B.; Al-Jadaan, A.; Al-Jibreen, H.; Li, J.; Lipa, J. A.; Lockhart, J. M.; Al-Suwaidan, B.; Taber, M.; Wang, S. Gravity Probe B: Final Results of a Space Experiment to Test General Relativity. *Phys. Rev. Lett.* **2011**, *106*, 221101.

(6) Bartlett, P. N.; Baumberg, J. J.; Birkin, P. R.; Ghanem, M. A.; Netti, M. C. Highly Ordered Macroporous Gold and Platinum Films Formed by Electrochemical Deposition through Templates Assembled from Submicron Diameter Monodisperse Polystyrene Spheres. *Chem. Mater.* **2002**, *14*, 2199–2208.

(7) Pugh, D. V.; Dursun, A.; Corcoran, S. G. Formation of nanoporous platinum by selective dissolution of Cu from Cu0.75Pt0.25. *Journal of Materials Research* **2003**, *18*, 216–221.

(8) Jacquet, P. A. Electrolytic Method for obtaining Bright Copper Surfaces. *Nature* **1935**, *135*, 1076.

(9) Abbott, A. P.; Capper, G.; McKenzie, K. J.; Ryder, K. S. Voltammetric and impedance studies of the electropolishing of type 316 stainless steel in a choline chloride based ionic liquid. *Electrochimica Acta* **2006**, *51*, 4420–4425.

(10) Ciovati, G.; Tian, H.; Gorcoran, S. G. Buffered electrochemical polishing of niobium. *Journal of Applied Electrochemistry* **2011**, *41*, 721–730.

(11) Piotrowski, O.; Madore, C.; Landolt, D. The Mechanism of Electropolishing of Titanium in Methanol-Sulfuric Acid Electrolytes. *J. Electrochem. Soc.* **1998**, *145*, 2362–2369.

(12) Sazou, D. Current oscillations and mass-transport control during electrodissolution of iron in phosphoric acid solutions. *Electrochimica Acta* *42*, 627–637.

(13) Andrade, L. S.; Xavier, S. C.; Rocha-Filho, R. C.; Bocchi, N.; Biaggio, S. R. Electropolishing of AISI-304 stainless steel using an oxidizing solution

originally used for electrochemical coloration. *Electrochimica Acta* **2005**, *50*, 2623–2627.
(14) Chang, S.-C.; Shieh, J.-M.; Dai, B.-T.; Feng, M.-S.; Li, Y.-H.; Shih, C. H.; Tsai, M. H.; Shue, S. L.; Liang, R. S.; Wang, Y.-L. Superpolishing for Planarizing Copper Damascene Interconnects. *Electrochem. Solid-State Lett.* **2003**, *6*, G72–G74.
(15) Kundig, K. J. A.; Dresher, W. H. Copper. In *Kirk-Othmer Encyclopedia of Chemical Technology*; John Wiley & Sons, Inc., Ed.; John Wiley & Sons, Inc.: Hoboken, NJ, USA, 2001.
(16) Lide, D. R. *CRC Handbook of Chemistry and Physics*; CRC Press: Boca Raton, FL, 2005.
(17) Gard, D. R.; Updated by Staff Phosphoric Acids and Phosphates. In *Kirk-Othmer Encyclopedia of Chemical Technology*; John Wiley & Sons, Inc., Ed.; John Wiley & Sons, Inc.: Hoboken, NJ, USA, 2005.
(18) Greenwood, N. N.; Thompson, A. 701. The mechanism of electrical conduction in fused phosphoric and trideuterophosphoric acids. *Journal of the Chemical Society (Resumed)* **1959**, 3485.
(19) Vilčiauskas, L.; Tuckerman, M. E.; Bester, G.; Paddison, S. J.; Kreuer, K.-D. The mechanism of proton conduction in phosphoric acid. *Nature Chemistry* **2012**, *4*, 461–466.
(20) Ebel, J.-P. Separation par chromatographie sur papier des oxyacides du phosphore. *Mikrochim Acta* **1954**, *42*, 679–700.
(21) Huhti, A.-L.; Gartaganis, P. A. The Composition of the Strong Phosphoric Acids. *Can. J. Chem.* **1956**, *34*, 785–797.
(22) Jameson, R. F. The composition of the strong phosphoric acids. *J. Chem. Soc.* **1959**, 752.
(23) Glarum, S. H.; Marshall, J. H. The Anodic Dissolution of Copper into Phosphoric Acid. *J. Electrochem. Soc.* **1985**, *132*, 2872–2878.
(24) Vidal, R.; West, A. C. Copper Electropolishing in Concentrated Phosphoric Acid. *J. Electrochem. Soc.* **1995**, *142*, 2689–2694.
(25) Aksu, S. Electrochemical Equilibria of Copper in Aqueous Phosphoric Acid Solutions. *J. Electrochem. Soc.* **2009**, *156*, C387–C394.
(26) Landolt, D. Fundamental aspects of electropolishing. *Electrochimica Acta* **1987**, *32*, 1–11.
(27) Du, B.; Suni, I. I. Mechanistic Studies of Cu Electropolishing in Phosphoric Acid Electrolytes. *J. Electrochem. Soc.* **2004**, *151*, C375–C378.
(28) Kojima, K.; Tobias, C. W. Interpretation of the Impedance Properties of the Anode-Surface Film in the Electropolishing of Copper in Phosphoric Acid. *J. Electrochem. Soc.* **1973**, *120*, 1202–1205.
(29) Chang, S.-C.; Shieh, J.-M.; Huang, C.-C.; Dai, B.-T.; Li, Y.-H.; Feng, M.-S. Microleveling mechanisms and applications of electropolishing on planarization of copper metallization. *J. Vac. Sci. Technol. B* **2002**, *20*, 2149.

(30) Padhi, D.; Yahalom, J.; Gandikota, S.; Dixit, G. Planarization of Copper Thin Films by Electropolishing in Phosphoric Acid for ULSI Applications. *J. Electrochem. Soc.* **2003**, *150*, G10–G14.

(31) Dau, H.; Limberg, C.; Reier, T.; Risch, M.; Roggan, S.; Strasser, P. The Mechanism of Water Oxidation: From Electrolysis via Homogeneous to Biological Catalysis. *ChemCatChem* **2010**, *2*, 724–761.

(32) Jones, S. F.; Evans, G. M.; Galvin, K. P. Bubble nucleation from gas cavities — a review. *Advances in Colloid and Interface Science* **1999**, *80*, 27–50.

(33) Vogt, H.; Balzer, R. J. The bubble coverage of gas-evolving electrodes in stagnant electrolytes. *Electrochimica Acta* **2005**, *50*, 2073–2079.

(34) Vignal, V.; Roux, J. .; Flandrois, S.; Fevrier, A. Nanoscopic studies of stainless steel electropolishing. *Corrosion Science* **2000**, *42*, 1041–1053.

(35) Singh, S.; Barden, W. R. T.; Kruse, P. Nanopatterning of Transition Metal Surfaces via Electrochemical Dimple Array Formation. *ACS Nano* **2008**, *2*, 2453–2464.

(36) Yuzhakov, V. V.; Chang, H.-C.; Miller, A. E. Pattern formation during electropolishing. *Phys. Rev. B* **1997**, *56*, 12608.

(37) Sagués, F.; Epstein, I. R. Nonlinear chemical dynamics. *Dalton Transactions* **2003**, 1201–1217.

(38) Manickam, D. Understanding Electrochemical Oscillations in Respect to the Step Formation on Nickel Metal. B. Sc. Thesis, McMaster University: Canada, 2011.

(39) Turing, A. M. The Chemical Basis of Morphogenesis. *Philosophical Transactions of the Royal Society of London. Series B, Biological Sciences* **1952**, *237*, 37 –72.

(40) El-Sayed, H.; Singh, S.; Kruse, P. Formation of Dimpled Tantalum Surfaces from Electropolishing. *Journal of The Electrochemical Society* **2007**, *154*, C728–C732.

(41) Singh, S.; Barden, W. R. T.; Kruse, P. Nanopatterning of Transition Metal Surfaces via Electrochemical Dimple Array Formation. *ACS Nano* **2008**, *2*, 2453–2464.

(42) Riddell, D. Nanopatterning of Electropolished Copper Surfaces. B.Sc. Thesis, McMaster University: Canada, 2009.

(43) Baig, S. Porous Copper Formation via Electropolishing. B. Sc. Thesis, McMaster University: Canada, 2010.

(44) Seo, Y. Atomic force microscopy and spectroscopy. *Reports on Progress in Physics* **2008**, *71*, 1–23.

(45) Egerton, R. F. *Physical principles of electron microscopy: an introduction to TEM, SEM, and AEM*; Springer, 2005.

(46) Levit, M. H. *Spin Dynamics: Basics of Nuclear Magnetic Resonance*; 2nd ed.; John Wiley & Sons, Ltd: The University of Southampton, 2008.

(47) Heide, P. V. D. *X-Ray Photoelectron Spectroscopy: An Introduction to Principles and Practices*; John Wiley & Sons, 2011.

(48) Fujiwara, H. *Spectroscopic Ellipsometry: Principles and Applications*; John Wiley & Sons, 2007.

(49) Smith, E.; Dent, G. *Modern Raman spectroscopy: a practical approach*; John Wiley and Sons, 2005.

(50) Kneipp, K.; Moskovits, M.; Kneipp, H. *Surface-enhanced raman scattering: physics and applications*; Springer, 2006.

(51) Ru, E. C. L.; Etchegoin, P. G. *Principles of Surface-Enhanced Raman Spectroscopy: And Related Plasmonic Effects*; Elsevier, 2008.

(52) Robinson, J. W.; Frame, E. M. S.; Frame, G. M. *Undergraduate Instrumental Analysis*; CRC Press, 2005.

(53) Shankar, P. N.; Kumar, M. Experimental Determination of the Kinematic Viscosity of Glycerol-Water Mixtures. *Proc. R. Soc. Lond. A* **1994**, *444*, 573–581.

(54) Chen, W.-H.; Lai, M.-Y.; Tsai, K.-T.; Liu, C.-Y.; Wang, Y.-L. Spontaneous Formation of Ordered Nanobubbles in Anodic Tungsten Oxide during Anodization. *J. Phys. Chem. C* **2011**, *115*, 18406–18411.